Contents lists available at ScienceDirect

Engineering Structures

journal homepage: www.elsevier.com/locate/engstruct

Highlights

A GA-based model updating procedure for the numerical simulation of FRCM-to-masonry bond

Engineering Structures xxx (xxxx) xxx

Giovanni Minafò*, Marielisa Di Leto, Gaetano Camarda, Lidia La Mendola

- FRCM-to-masonry bond is studied.
- A simplified FE model is proposed.
- A GA-based model updating procedure is implemented.
- Comparisons with experimental results prove the efficacy of the procedure.

Contents lists available at ScienceDirect

Engineering Structures

journal homepage: www.elsevier.com/locate/engstruct

A GA-based model updating procedure for the numerical simulation of FRCM-to-masonry bond

Giovanni Minafò *, Marielisa Di Leto, Gaetano Camarda, Lidia La Mendola

Universita degli Studi di Palermo, Dipartimento di Ingegneria, Viale delle Scienze, Ed.8, Palermo, 90128, Italy

ARTICLE INFO

Keywords:
FRCM
Bond
Genetic Algorithm
Interface
Model updating

ABSTRACT

The characterization of the constitutive mechanical behaviour of Fabric Reinforced Cementitious Composites (FRCM) is a widely discussed topic in the scientific community. Several research studies pointed out the difficulties in assessing reliable constitutive laws able to reproduce the local phenomena inner in the mechanics of FRCM materials. This paper presents the proposal of a model updating procedure based on a Genetic Algorithm (GA), able to obtain the parameters to be used for a simplified numerical modelling of the fabric-to-matrix interface. The procedure is applied to a truss-based Finite Element (FE) model, and it aims to minimize the difference between the simulations and the experimental results. The calibration procedure is performed against a large experimental database of bond tests in FRCM-to-masonry assemblies, allowing to express the model parameters as a function of geometrical and mechanical characteristics of the FRCM.

1. Introduction

The scientific community has recently focused great attention on the characterization of the constitutive mechanical behaviour of Fabric Reinforced Cementitious (FRCM) Composites. This growing interest is due to the several potential applications of these materials in the field of retrofit and restoration of historical structures, with particular reference to masonry buildings [1,2]. FRCM composites consist of high-strength fibres, such as carbon or glass, embedded in a cementitious matrix. The fibres provide tensile strength [3,4] and ductility to the composite, while the cementitious matrix serves as a binder and provides resistance against environmental conditions. The benefits of using FRCM composites for structural retrofitting include durability and corrosion resistance, compatibility with the support, fire resistance, easiness and low installation costs, and for these reasons, several research works were addressed to study the application of FRCM for structural retrofitting applications, especially in masonry structures [5–9].

The huge amount of research performed during the last decade aiming in characterizing the mechanical performances of FRCM materials pointed out that the evaluation of the bond behaviour between the composite and the masonry substrate is of crucial importance for ensuring the effectiveness of the intervention. In fact, when the FRCM strip is loaded in tension, the matrix is subjected to the formation of cracks and the transmission of the stress between the mortar and the fibre is related to the interface between the two phases [10,11]. In this field, several experimental studies were developed, studying the role of the different variables affecting the bond behaviour, such as the nature and the composition of the FRCM [11–13], the effect of the bond length, the role of test set-up [14–16] or the durability of the system [17]. The great attention on this subject is proved by the wide database of experimental results, which can deduced from direct shear bond test presented in the literature.

Despite the great amount of experimental research works performed in this field, fewer modelling strategies were proposed to predict the complex stress-transfer mechanisms that develop at the fabric-to-matrix and composite-to-substrate level. All of these studies are based on some assumptions on the constitutive behaviour of the interfaces. Grande and Milani [18] proposed a spring model approach calibrated on some experimental results available in the literature, and assuming an interface law approach with a bi-linear relationship formally equivalent to the parabolic/exponential law proposed in [19]. Bertolesi et al. [20] analyzed the efficiency of different modelling approaches which specifically account for the interaction between the mortar and the fabric. The study was performed by simulating some case studies deduced from the recent literature and by considering shear stress-slip laws derived from experimental records. Calabrese et al. [21] solved analytically the problem of bond by adopting a rigid-softening cohesive law for the interface, deducing the parameters characterizing this law from proper experimental results. Nerilli et al. [22] adopted a micromechanical approach to model tensile and bond behaviour of FRCM systems. The researchers introduced interface finite elements inside and between the FRCM constituents and took into account damage, friction and the

* Corresponding author.
E-mail address: giovanni.minafo@unipa.it (G. Minafò).

https://doi.org/10.1016/j.engstruct.2024.117512
Received 11 September 2023; Received in revised form 7 December 2023; Accepted 8 January 2024

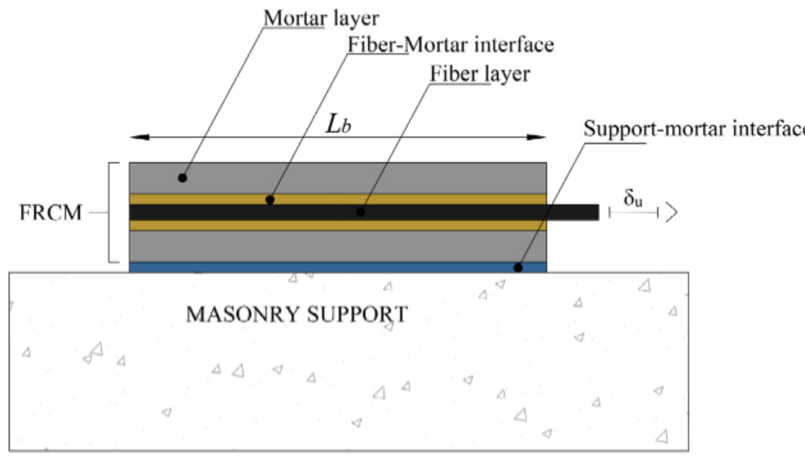

Fig. 1. Geometry of the case studies.

unilateral contact for simulating the opening of cracks and slip between the fibres and the mortar. Grande and Milani [23] proposed a procedure for calculating approximate shear stress-slip laws for numerically simulating the local bond behaviour of FRCM systems at the fabric-to-mortar interface. The procedure was based on the outcomes of experimental bond tests with the governing equations of the model proposed by the same researchers in [18].

It is evident from the literature that the solution of the problem of bond is strictly related to the assumptions made at the fabric-to-matrix and matrix-to-support interface. Despite the scientific community proposed some material laws i.e. pure brittle linear, rigid-softening, trilinear or Thorenfeldt-like law [19], the estimation of the parameters able to define this law still remains an open problem. All the research works calibrated the parameters based on their experimental data or on a limited number of tests presented in the literature. As a result, the calibration of a predictive numerical model for simulation purposes still remains difficult.

Aiming to cover this lack, this paper aims to propose a broad-band calibration of interface parameters for the simulation of shear bond tests by taking advantage of a model-updating procedure based on a Genetic Algorithm (GA).

A simplified Finite Element (FE) model is initially formulated as a reference model for simulating shear bond tests. This model is specifically adopted for reducing the computation time, as it uses truss elements and zero-length springs for modelling the two phases and the interfaces respectively. The model allows the possibility of simulating cracks in the matrix and the relative slip at the interface. Deterministic parameters are assumed for the constituent materials - matrix and fabric- while the model uncertainties are enclosed in six parameters defining the constitutive laws of the two interfaces. The updating procedure is therefore set by writing a protocol based on a GA. The optimization aims to minimize an error index, which measures the gap between the Force-Slip response experimentally observed and that obtained numerically, in terms of maximum force, stiffness and dissipated energy.

All the procedure and the reference model is entirely implemented in an all open-source environment, which takes advantage of OpenSeesPy [24] for the simulations and Python [25] for the procedure implementation, making up an unique environment for pre and post-processing the results. The calibration is therefore performed against a large database of experimental data recorded in the literature, allowing to make some general conclusions on the obtained results and proposing some laws for general simulation purposes.

2. Reference FE model

The numerical model aims to reproduce the results of shear bond tests on FRCM-to-masonry samples, as shown in Fig. 1. In these tests the system is loaded through the application of a load or displacement history at the free fibre end and transferred to the masonry support through the composite, bonded to the masonry for a bond length L_b.

2.1. Formulation

The numerical model here adopted is based on the use of a series of truss elements connected through shear springs (Fig. 2), based on a previous simplified model presented in the literature [26,27]. This choice is made in order to minimize the computation time, due to the fact that generally, a model updating procedure or an optimization problem requires several simulations.

It is here clarified that the current model takes advantage of standard elements available in the OpenSeesPy libraries. Anyway, the formulation is here presented in order to give the reader the possibility of implement the model in a generic environment or to perform an "ad hoc" implementation.

Truss elements are adopted for modelling the two phases, fabric and matrix, while pure shear stiffness elements are considered for simulating in discrete manner the fabric-to-matrix and the matrix-to-support interfaces. Three rows of trusses are modelled for making up the geometry, one for modelling the matrix layer on the top, one for including the fibre fabric and the third row on the bottom for considering the lower layer of mortar. The two orders of trusses simulating the matrix are linked to the series of central fabric trusses through shear springs in correspondence of the nodes. Finally, the lower row of mortar trusses are connected to restrained supports, which consider that the stone or masonry support is assumed to be constrained to zero displacement. This connection is made with a further row of shear springs, as depicted in Fig. 2, which simulate the interaction between the FRCM and the masonry. Additionally, axial spring elements were also added in series at the ends of each matrix truss. These springs, namely "brittle hinges", were introduced to simulate crack opening in the mortar. In fact a rigid-brittle constitutive law is assigned to these elements, allowing the axial force dropping to zero after that tensile strength of the matrix is reached. Each brittle hinge's length $L_{brittle}$ was calibrated for each analysis to be equal to a certain portion of the truss element's length.

In this way, the local stiffness matrix of the generic "j" element is a 4×4 matrix expressed as follow:

$$\tilde{\mathbf{K}}^j = \begin{pmatrix} \rho_a^j & 0 & -\rho_a^j & 0 \\ 0 & \rho_s^j & 0 & -\rho_s^j \\ -\rho_a^j & 0 & \rho_a^j & 0 \\ 0 & -\rho_s^j & 1 & \rho_s^j \end{pmatrix} = \begin{pmatrix} \tilde{\mathbf{K}}_{ii}^j & \tilde{\mathbf{K}}_{ik}^j \\ \tilde{\mathbf{K}}_{ki}^j & \tilde{\mathbf{K}}_{kk}^j \end{pmatrix} \quad (1)$$

being ρ_a^j and ρ_s^j the axial stiffness and the shear stiffness of the element respectively.

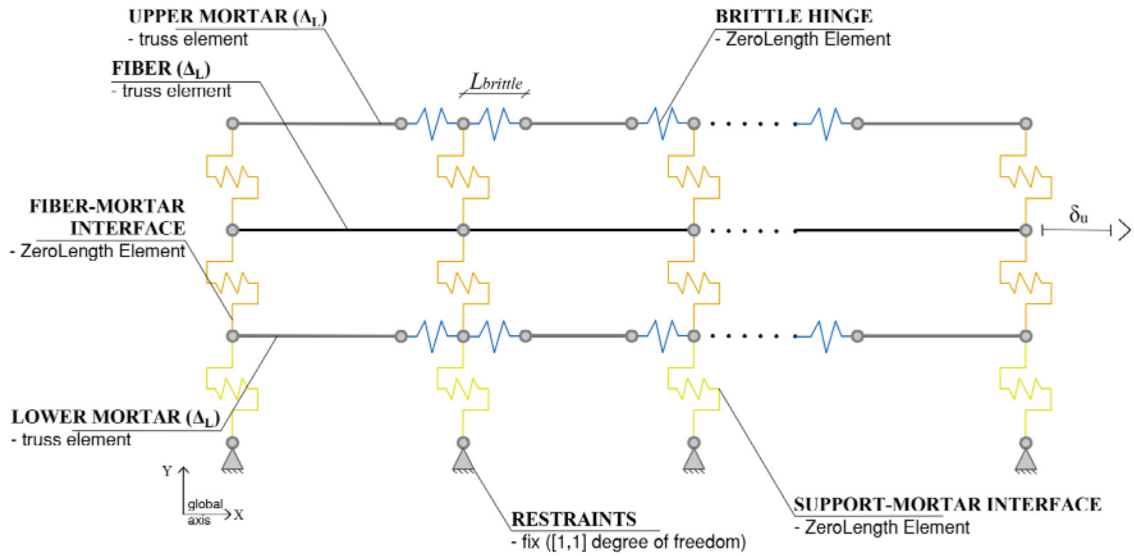

Fig. 2. Reference model.

All the fabric and mortar elements are assumed to behave elastically with a pure brittle constitutive law. Only the definitions of the elastic modulus (E_f and E_m) and the cross section (A_f and A_m) are required to determine the stiffness of these parts. A_f was assumed equal to the mortar's nominal thickness, while the fabric's typical dry fibre cross-section was taken for calculating A_f.

In this way, the shear stiffness of generic "j" truss element is equal to zero -i.e. $\rho_s^j = 0$-, while the axial stiffness is easily defined as

$$\rho_{a,f}^j = E_f A_f / l_j \quad \text{for} \quad j = 1 \ldots n_f \tag{2a}$$

$$\rho_{a,m}^j = E_m A_m / (l_j - L_{brittle}) \quad \text{for} \quad j = (n_f + 1) \ldots (n_m - n_f) \tag{2b}$$

being l_j the length of the truss, that is equal for all the truss elements in the model. Finally, n_f is n_m are the tag number of truss modelling the fabric and the tag number of that of the mortar matrix respectively. It has been shown that the "brittle hinges" have a little impact on the stiffness of each matrix truss. In fact, being its stiffness equal to infinite, the assembled stiffness of the three trusses along the length l_j is related only to the deformable part.

All the shear springs used to define the interface have only shear stiffness -i.e. $\rho_a^j = 0$-. This last was deduced by multiplying the continuum stiffness for the area between two successive nodes. Therefore, the initial elastic stiffness is set equal to

$$\rho_{s,i}^j = K_{fm} \quad \text{for} \quad j = 1 \ldots n_f \tag{3a}$$

$$\rho_{s,s}^j = K_{sm} \quad \text{for} \quad j = (n_f + 1) \ldots (n_m - n_f) \tag{3b}$$

being K_{fm} the discrete form of the tangent stiffness of the fabric-to-mortar interface elements and K_{sm} the discrete form of the tangent stiffness of the mortar-to-support interface elements. It is worth noting that the subscript "i" and "s" denote the fibre-to-matrix and the matrix-to-support interface.

All the nodes have the same Y-coordinate, assumed equal to 0 in the current implementation, and therefore it is all defined along a line. Therefore the model work in one direction -i.e. 1D model-.

Consequently, the transformation matrix for all the trusses is equal to a 4 × 4 identity matrix, considering the direction cosines of the unit vector along the element. While differently, for all the shear spring elements, it assumes the following form

$$\Lambda_j = \begin{pmatrix} 0 & -1 & 0 & 0 \\ 1 & 0 & 0 & 0 \\ 0 & 0 & 0 & -1 \\ 0 & 0 & 1 & 0 \end{pmatrix} \tag{4}$$

Hence, projecting the local stiffness matrix in the global reference system in the form $\mathbf{K^j} = \mathbf{\Lambda_j^T \tilde{K}^j \Lambda_j}$, the global stiffness matrix at element level becomes the following matrix:

$$\mathbf{K^j} = \begin{pmatrix} K_{ii}^j & 0 & K_{ik}^j & 0 \\ 0 & 0 & 0 & 0 \\ K_{ki}^j & 0 & K_{kk}^j & 0 \\ 0 & 0 & 0 & 0 \end{pmatrix} = \begin{pmatrix} K^j & 0 & -K^j & 0 \\ 0 & 0 & 0 & 0 \\ -K^j & 0 & K^j & 0 \\ 0 & 0 & 0 & 0 \end{pmatrix} \tag{5}$$

being $K^j = \rho_a^j$ for truss elements and $K^j = \rho_s^j$ for spring elements.

As consequence of the stability of the system only along the horizontal, namely x, direction, there are two rows of zeros in the global stiffness matrix. This assumption simplify noticeably the problem, in fact if the global stiffness matrix of the system is assembled, all the zero rows can be deleted, and the system is condensed to a single equilibrium equation for each node, to be written for the ith node in the form

$$\delta_{x,i} \sum_{j=1}^{N} K^j - \delta_{x,k} \cdot \sum_{j=1}^{N} K^j = \begin{cases} 0 & \text{for unloaded node} \\ \lambda_z F_i & \text{for loaded node} \end{cases} \tag{6}$$

being $\delta_{x,i}$ the horizontal displacement of the i node, $\delta_{x,k}$ that of the kth node connected to i, N the number of elements connected to i, F_i the horizontal force applied to the i node and λ_z the load factor multiplier. Finally the global stiffness matrix K_G is a $n \times n$ matrix, being n the number of free nodes in the model, which summarizes the coefficients expressed by the system of equilibrium equations, as expressed by Eq. (6). The final compact form of the equilibrium equation of this system is therefore written as

$$\mathbf{K_G} \cdot \delta = -\mathbf{f^0} \tag{7}$$

where $\mathbf{f^0}$ is the vector of nodal loads and δ is the vector including all the unknown displacements.

2.2. Materials and interfaces

The developed model requires easily only the definition of uniaxial material laws, and the assumptions made in the current study are resumed in Fig. 4.

Matrix and fibre were assumed to behave elastically with a pure brittle constitutive law. All the material parameters concerning the fabric and the mortar were assumed as deterministic, i.e. known a priori. In particular, the fabric was assumed to react only in tension

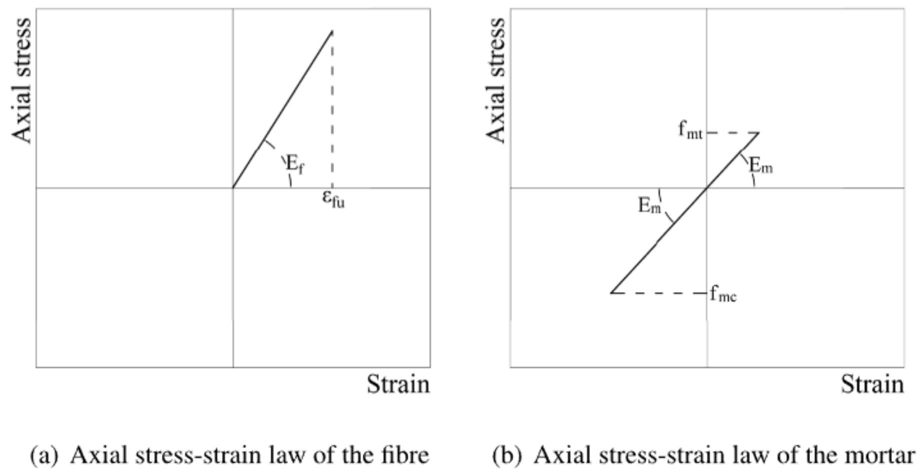

Fig. 3. Adopted constitutive models.

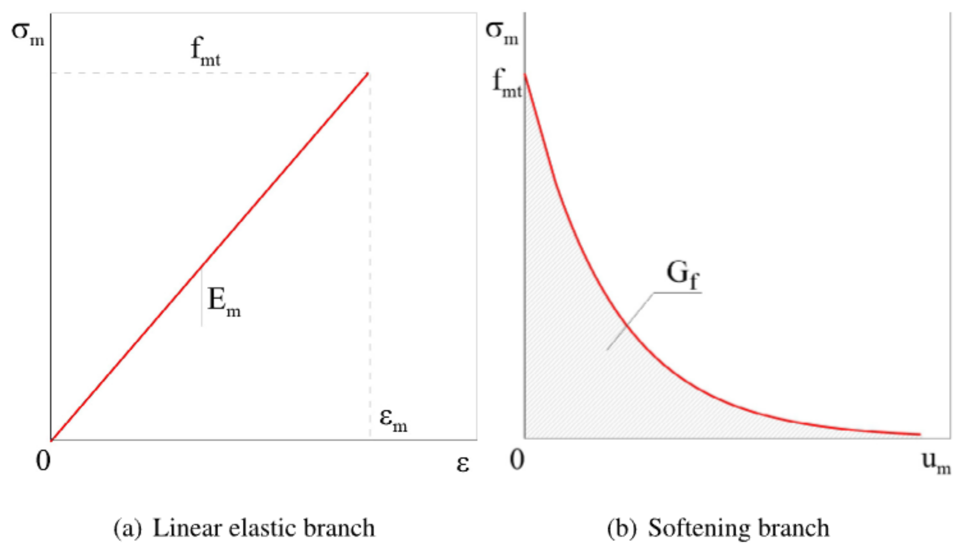

Fig. 4. Elastic-softening mortar constitutive behaviour.

with elastic modulus E_f and ultimate tensile strain ε_{fu} (Fig. 3(a)). Mortar was assumed working linear elastically in tension and compression with equal elastic modulus E_m, while f_{mt} and f_{mc} are compressive and tensile strength (Fig. 3(b)). It is worth noting that in absence of more detailed indications, the tensile strength of the matrix was assumed as $f_{mt} = 0.1 f_{mc}$, depending on the compressive strength which is more usually given in the experimental works in the literature.

Similarly, when no indications are provided for the elastic modulus of the matrix, the following expression [28] was used for deriving its value

$$E_m = 22000 \left(\frac{f_{mc}}{10} \right)^{(1/3)} \tag{8}$$

where f_{mc} is expressed in MPa.

Consequently, a brittle constitutive behaviour was assigned to brittle hinges, for which the maximum stress drops to zero when mortar tensile strength is reached. This type of constitutive behaviour simplifies the model calibration, while also taking into account the fact that it is already difficult to directly assess the mortar tensile behaviour. It is worth noting that more complex constitutive models of the mortar are available in the literature,such as the introduction of a softening ruled by a certain fracture energy G_f (Fig. 4).

This softening branch follows usually an exponential relationship between mortar tensile stress σ_m and mortar displacement u_m (which represents the concentrated crack width) at the local origin of the crack, in the form:

$$\sigma_m = f_{mt} e^{-\frac{f_{mt}}{G_f} u_m} \tag{9}$$

The constitutive representation of the mortar softening in tension through exponential functions is a well known numerical strategy that can be widely found in the literature [29–31]. On the other hand, it has been demonstrated in Yuan and Milani [31], that the adoption of such a law usually affects only the first cracking stage. In fact, under this assumption, the crack width increases progressively, allowing to see a snap-back of the global curve until the crack can be considered fully developed, while differently a sudden vertical drop is observed if a pure elastic brittle law is considered. However, for the sake of clarity, an example is reported below in the section “Results and discussions” for clarifying this aspect.

The uncertainties of the current FE model were here assumed in the parameters which define the constitutive laws to be used for the two interfaces. Fig. 5 shows the shapes assumed for the constitutive laws of the two interfaces, highlighting the unknown parameters to be calibrated.

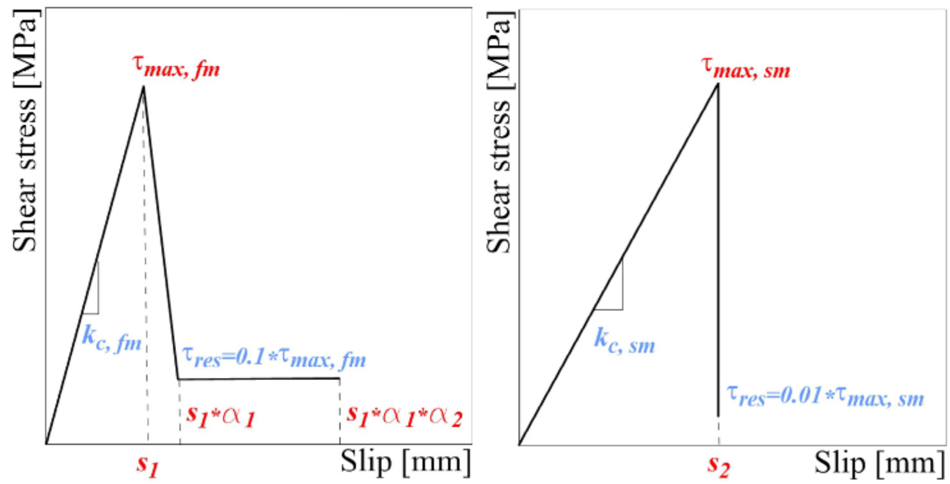

(a) Shear stress-slip of the fabric-to-matrix interface (b) Shear stress-slip of the matrix-to-support interface

Fig. 5. Constitutive models parameters.

In particular, a pure shear trilinear model was assumed for the fabric-to-matrix (fm) interface (Fig. 5(a)), while a pure brittle elastic law was considered for the matrix-to-support (sm) interface (Fig. 5(b)). The maximum stresses in the two models are denoted as $\tau_{max,fm}$ and $\tau_{max,sm}$, while s_1 and s_2 the corresponding values of slip.

It is additionally assumed that the fm interface has a residual shear stress due to friction τ_{res}. Its value is here imposed as a fraction of the maximum stress, equal to 10% for the fm interface and 1% for the sm interface. It is here evidenced that the proposed model could take into account also the presence of a normal stress acting on the interfaces, which is a common situation when the FRCM is applied to curved surfaces. Anyway, this would results in an additional unknown parameter or on a further correlation to be performed between the maximum stress and the acting normal force. Further investigations should be addressed in this sense. It is here clarified that no residual shear stress due to friction was assumed in the constitutive law of the sm interface due to the fact that the no specimen listed in the database failed due to the crisis of the support interface, and this occurrence -i.e. cohesive failure of the support- is quite uncommon in FRCM-to-masonry bond tests. On these bases, adding a residual stress in the vector of unknown parameters would result in complicating the algorithm and its convergence time.

Finally, the coefficients α_1 and α_2 are two scalar parameters which allow to calculate the characteristic points of the constitutive laws of the fm interface as a function of peak parameters.

3. Model updating procedure based on the GA approach

3.1. Encoding

The first step of an optimization problem is to define an individual $\vec{V}_d$, i.e. a vector including a number of unknown parameters, these last representing a possible solution of the problem. These parameters in the field of GAs are called “chromosomes” and, in this specific case, six parameters are assumed enough to define the constitutive behaviour of the fibre-to-matrix and matrix-to-support interfaces. In this way, individuals are defined in the following form:

$$\vec{V}_d = [\tau_{max,fm}, \tau_{max,sm}, s_1, s_2, \alpha_1, \alpha_2]^T \tag{10}$$

The symbols in Eq. (10) are referred to Fig. 5. The existence domain of the single genes is limited in the search space. In particular, the maximum shear stress $\tau_{max,fm}$ is assumed to exist in the domain limited by the tensile strength of the matrix, in the form

$$\tau_{max,fm} \in [0, f_{mt}] \tag{11}$$

Similarly, the maximum stress at the sm interface $\tau_{max,sm}$ was limited by the lower value of tensile strength between the masonry support f_{ts} or the matrix

$$\tau_{max,sm} \in [0, min(f_{mt}, f_{ts})] \tag{12}$$

For the two parameters α_1 and α_2, values greater than 1 were assumed. The lower bound values of the parameters correspond to the definition of a brittle interface (Fig. 5). The existence of these parameters is search in the following domains

$$\alpha_1 \in [1, 10] \tag{13}$$

$$\alpha_2 \in [1, 5] \tag{14}$$

which were estimated on the basis of previous simulations.

3.2. Fitness function

As well known, the optimization procedures require the definition of an objective function, called fitness function, and generally, a model updating procedure is performed for minimizing the differences between the numerical predictions and the experimental outcomes. For this reason, the fitness function of the current optimization problem was represented by the magnitude of a vector $\vec{F}$ defined in the space of three global prediction errors.

$$\vec{F} = [EP_F, EP_k, EP_E]^T \tag{15}$$

The components of $\vec{F}$ denotes the percentage errors in terms of three features characterizing the Load vs. Slip curves: maximum force F_{max}, stiffness k, corresponding to the slope of the first linear branch, and overall area E enclosed by the curve, which corresponds to the energy dissipated during the test. These quantities can be related to the experimental curve and denoted with the subscript *exp* or to the numerical response with the subscript *num* (Fig. 6).

In this way, the three components of $\vec{F}$, measuring the accuracy of the simulation, can be evaluated as:

$$EP_F = \left| \frac{F_{max,num} - F_{max,exp}}{F_{max,exp}} \right| \tag{16}$$

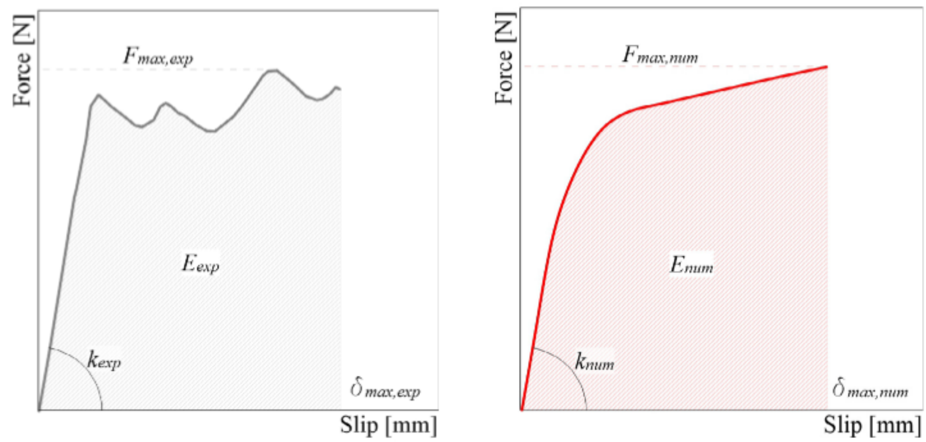

(a) Experimental Force vs. Slip curve (b) Numerical Force vs. Slip curve

Fig. 6. Fitness function parameters.

$$EP_k = \left|\frac{k_{num} - k_{exp}}{k_{exp}}\right| \tag{17}$$

$$EP_E = \left|\frac{E_{num} - E_{exp}}{E_{exp}}\right| \tag{18}$$

meaning EP_F, EP_k and EP_E the percentage errors in terms of force, stiffness and dissipated energy.

Finally, the fitness function is numerically evaluated as the magnitude of $\vec{F}$:

$$\left|\vec{F}\right| = \sqrt{(EP_F)^2 + (EP_k)^2 + (EP_E)^2} \tag{19}$$

It is worth noting that if the coordinate space is defined by the percentage errors (Eq. (16), (17), (18)) -namely EP space-, each single generation can be represented as a point P in this space, as represented in Fig. 7. In this way, the vector $\vec{F}$ coincides with the position vector of P, and it can be expressed as

$$\vec{F} = EP_F \cdot \hat{e}_x + EP_k \cdot \hat{e}_y + EP_E \cdot \hat{e}_z \tag{20}$$

being $\hat{e}_x$, $\hat{e}_y$, $\hat{e}_z$ versors of the three Cartesian axes.

The fitness function Eq. (19) is therefore alternatively defined as the length of the position vector

$$\left|\vec{F}\right| = \sqrt{\vec{F} \cdot \vec{F}} = \sqrt{(EP_F)^2 + (EP_k)^2 + (EP_E)^2} = F \tag{21}$$

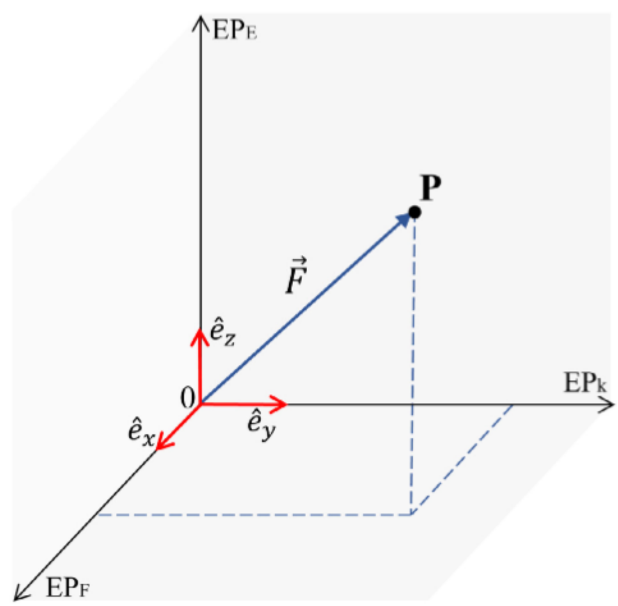

Fig. 7. Geometric interpretation of F.

In this way, the function F can be considered a metric of the simulation error, and its minimization is the target of the model updating procedure. It is here clarified that several expressions of the error metric can be defined, and usually in the field of GA, the match of a simulation is expressed by the root mean square error between the experimental observation and the prediction. However, this approach is not here considered due to the fact that such an approach would require that the model should follow the experimental trend along the experimental curve. In this way, the simulation would be “forced” to follow the irregularities often recorded in a test (see Fig. 6(a)). It is clear that this approach is not suitable for a simplified model, as that adopted in the current work, and generally a predictive model in the field of structural mechanics can be considered reliable if the global predictions in terms of maximum load capacity, stiffness and dissipated energy are close to the experimental records.

It is here clarified that the fitness function here presented considers equally weighted errors on the initial stiffness, resistance and dissipated energy (Eq. (21)). The possible assignment of different weights to the errors could modify or improve the convergence of the procedure. Anyway, this would require a preliminary calibration of the weights, in order to assess the influence of each error on the global response. In the spite of keeping a general purpose model updating procedure, it is here assumed to give the same weight to the estimation of maximum load, stiffness and dissipated energy.

3.3. Statement of the problem and algorithm workflow

The definition of the fitness function as in Eq. (21) allows to identify the target of the algorithm, i.e. finding the parameters which allow the minimization of the length F, which measures the overall simulation error. In this way, the model updating procedure can be expressed in the following optimization form:

$$\begin{aligned} \min_{\vec{V_d}} \quad & F \\ \text{s.t.} \quad & \mathbf{K_G} \cdot \delta + \mathbf{f^0} = 0 \end{aligned} \tag{22}$$

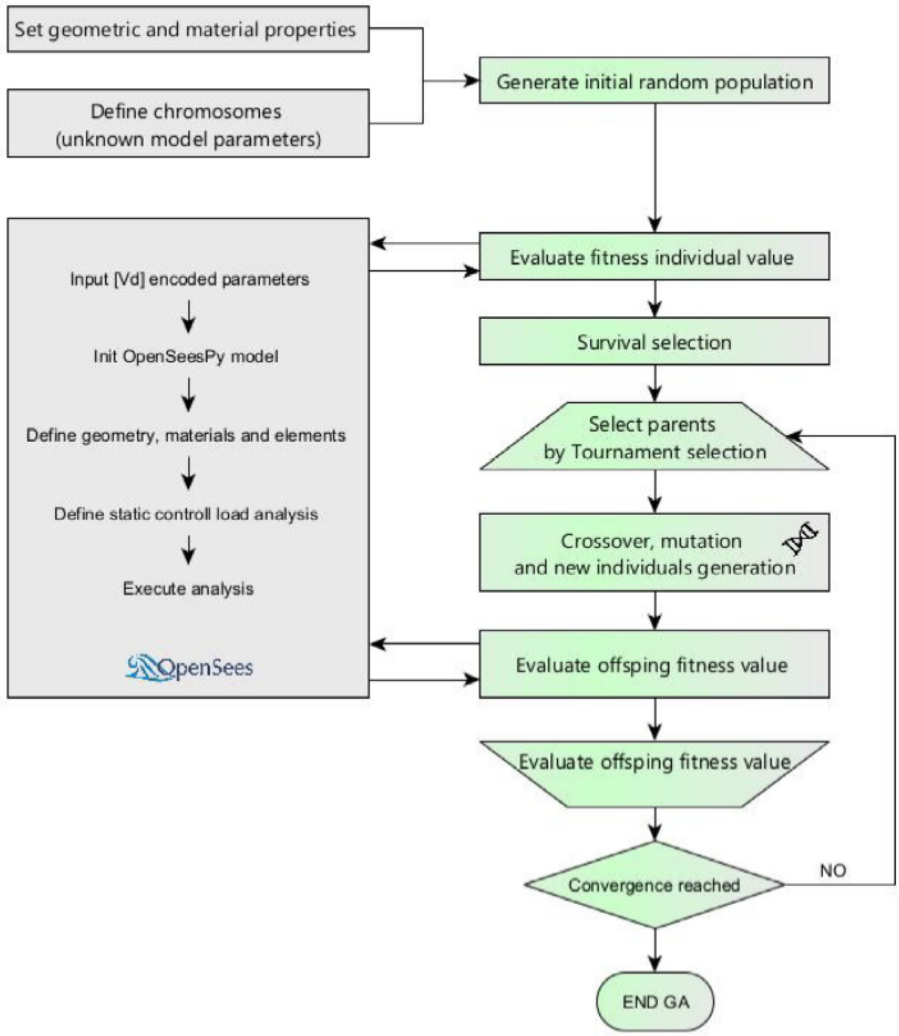

Fig. 8. Genetic Algorithm flowchart.

As discussed above, the problem expressed by Eq. (22) is here solved by adopting a GA approach.

The procedure implemented and the algorithm workflow is resumed in the flowchart reported in Fig. 8, which shows the interaction between the FE model and the calibration procedure. Unlike many optimization algorithms, a GA method has a higher probability of converging to a global optimal solution than a gradient-based method.

A GA is a population-based, probabilistic technique that operates to find a solution to a problem from a population of possible solutions [32] through the application of the principles of evolutionary biology to computer science [33,34].

The current GA starts from generating an initial population size of 14 individuals, randomly generated- i.e. 14 FE models each one with an assigned $\vec{V}_d$ (Eq. (10)). The population size is kept constant at each cycle, and its dimension was calibrated observing the computation time and the rapidity of convergence.

In a second step, after running the analyses, the fitness of each individual F is calculated and the best individuals -i.e. the parents- are selected for making the new combinations.

Among the different selection operators, the tournament selection approach was here chosen, as schematically explained in Fig. 9. This method runs a series of tournament inside the population, individuals are selected and the best is chosen by its fitness value. In this way, k individuals are chosen from the population, sorted according to fitness value, and the best one is taken for mating. The value of k, called tournament size, was chosen considering that a very large value allows for fast convergence with a rougher fit, while a very small value implies a longer analysis time with a better fit. In the present work, a tournament size value of $k = 7$ was chosen.

The Blend Crossover technique was chosen to generate the offsprings. The crossover process involves generating, from the parents' chromosomes, ranges from which to stochastically choose the values to be assigned to the new individual's genes (Fig. 10). Specifically, by defining the ith gene of the two parents with x_i and y_i, the new gene is chosen stochastically within an interval defined as follows (with $x_i < y_i$):

$$[x_i - \alpha(y_i - x_i), y_i + \alpha(y_i - x_i)] \tag{23}$$

where α is a real number that allows the domain of existence of the new gene to be extended and to which a value of 0.1 has been assigned.

Finally, a mutation operator was introduced in order to warrant the genetic diversity among the population, avoiding the algorithm to find local minimum solutions and searching for a global minimum value. In this case, a Gaussian mutation was assumed, in which a gene is randomly changed by adding a new value extracted from a Gaussian distribution. The mutation is controlled by the mutation rate, which expresses the probability of each individual to be changed within a generation. A preliminary calibration of this parameter was performed, as shown in Fig. 11, which reports the effect of the mutation rate on the convergence of the analysis. As it can be noted, low values of

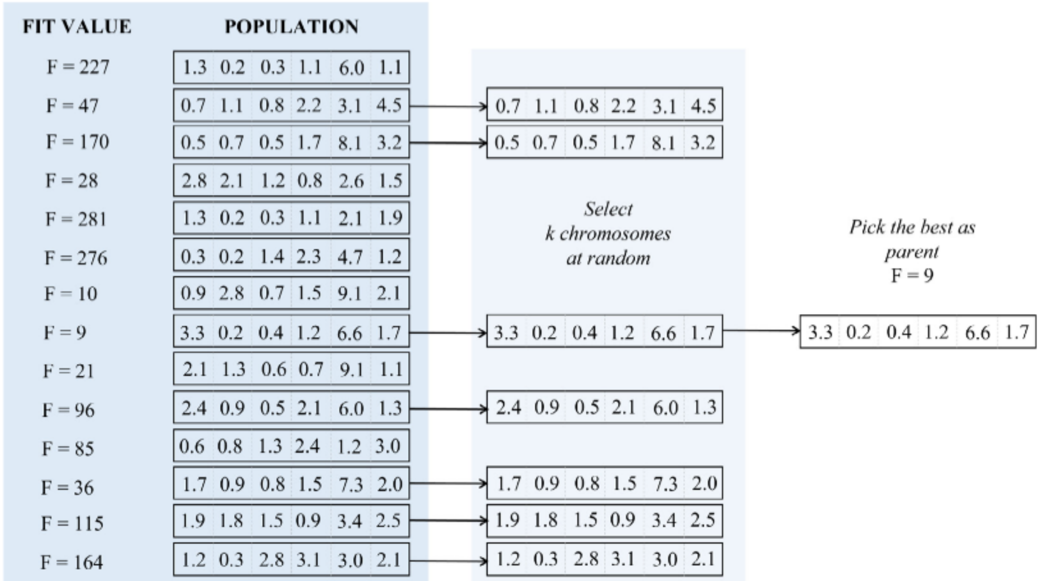

Fig. 9. Tournament selection procedure.

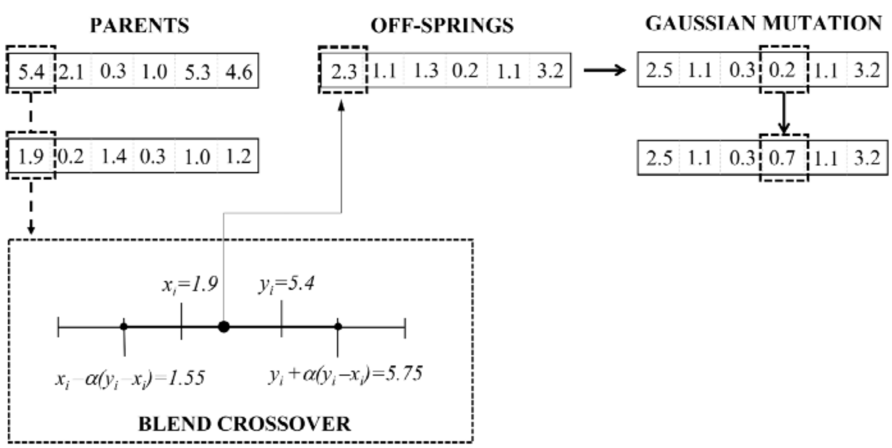

Fig. 10. Example of crossover, offspring generation and mutation.

the mutation rate imply a fast convergence, but with the possibility of identifying local minimum points, while a greater value prevents the population from converging towards the optimal solution and algorithm could be considered as a random search environment.

It is evident from the analysis that the value of 0.5 allows the faster convergence, due to the fact that the fitness value keeps constant from the 25th to the 170th generation. Therefore the value of 0.5 was selected for performing the analyses.

4. Model implementation

The entire procedure is implemented in Python v3.9 [25] environment, taking advantage of the OpenSeesPy [24] framework for the structural modelling and FE analysis, while the numpy [35] and matplotlib [36] libraries were used for data analysis and plotting. The overall framework is developed following the workflow shown in Fig. 12.

Concerning the FE model, an automatic procedure was developed for creating the geometry. Some *classes* are introduced for a better implementation of nodes and elements object's, and each one of them is identified between *string* tags. The implemented *classes* also include some methods using OpenSeesPy recorders to retrieve the output data at each step of the analysis.

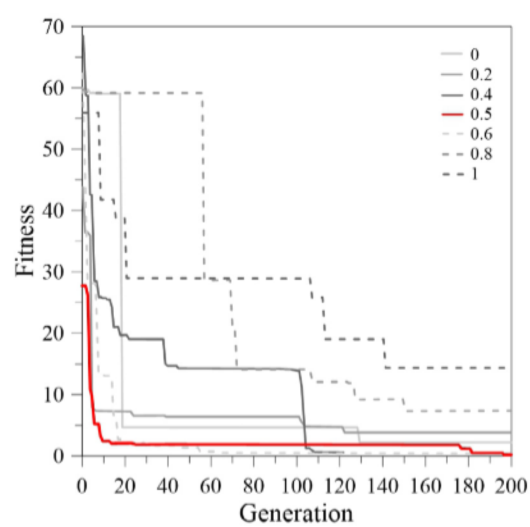

Fig. 11. Effects of mutation ratio variation.

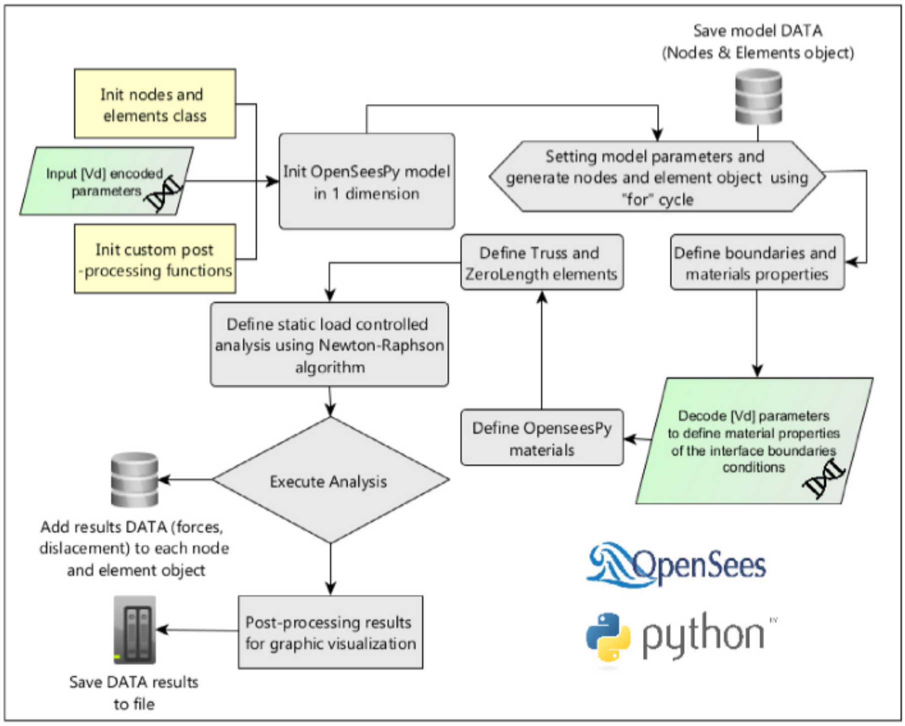

Fig. 12. Workflow and architecture of the developed software.

A specific plot function has been programmed to visualize easily the implemented nodes and element types colored by tags for a better understanding of the model discretization, but the output image of this function is not hereby reported.

Following this pre-processing stage, the OpenSeesPy framework is initialized using the mechanical properties of the mortar and fibre, the specimen's geometrical parameters, and the number of discretization nodes as inputs. All the geometric nodes are implemented using a "*for loop*" dividing the model as a ratio of specimen length by the node number. The connectivity of the elements is formed, the tags are allocated, and the nodes of the *object* are initialized during this stage. To simulate the masonry layer and apply the boundary conditions in the OpenSeesPy framework, pinned support is applied to base nodes (see in Fig. 2), and then material properties and *Truss* and *ZeroLength* elements are defined. The constitutive laws of assigned materials are shown in Fig. 4, they mostly use elastic material with strain or stress limits (for mortar and fibre) and non-linear with negative slope material for the interface layer. At this stage, the elements' geometry and mechanical characteristics are known, and the analysis algorithm may be used to carry out the analysis.

The rightmost fibre node is subjected to a δ_u displacement that is raised until it achieves the desired displacement U_{max} during the execution of a non-linear static analysis under displacement control, which uses the Newton–Raphson method to solve the non-linear system of equations. To make the post-processing analysis for both the global and local response less difficult, the output results for each step of the analysis are stored inside each node and element objects in terms of displacements and reaction forces.

5. Results and discussion

5.1. Example of application

Fig. 13 shows an example of GA calibration based on an experimental result from Calabrese et al. [37]. It consists of a carbon fibre textile with yarns spaced at 10 mm in the center in both longitudinal and transversal directions. The width and thickness of the single yarn are 5 mm and 0.084 mm, respectively. The tensile strength of the fabric obtained by direct tensile testing is 1944 MPa, the ultimate strain is 0.0095, and the elastic modulus is 203 GPa. The matrix consists of cement-based mortar with average compressive and flexural strength of 25 MPa and 6.1 MPa, respectively. The substrate is made by clay bricks and mortar joints with a nominal thickness of 10 mm and compressive strength of the mortar lower than 5 MPa. The FRCM strips applied to the substrate have a thickness of 8 mm, a bonded width of 60 mm, and a bonded length of 210 mm.

The input parameters of the model were the geometric and mechanical characteristics of the sample. The mesh size is defined by setting equal to 50 the number of elements for each series of truss element. Taking into account the geometry of the sample under consideration, dividing the length by the number of elements, the mesh size is 4.2 mm. The model therefore consists of 150 truss elements, divided as follows: 50 upper mortar, 50 fibres, 50 lower mortar. At the ends of each mortar truss element, two ZeroLength elements are allocated for a total of 200 elements. While for the simulation of the interfaces, another 153 ZeroLength elements are inserted: 102 to constitute the two fibre-to-matrix interfaces and 51 to simulate the matrix-to-support interface. The simulation was conducted in displacement control, imposing the displacement at the last node of the fibre. The ultimate displacement was imposed equal to the average displacement recorder during the experimental test, while the load increment was set equal to 0.05 mm.

Fig. 13(a) shows the best solution obtained at different generations in terms of Load-Slip curve. It is worth noting as the simulation converges rapidly to the optimized best-matching solution, and just after 25 generations the numerical response is close to the experimental solution. Fig. 13(b) shows the trend of the fitness function and the three percentage of errors (Eqs. (16), (17), (18)) as a function of the number of generations. In this case, it is shown as the error is mainly due to the force estimation, being this last the greater value among the three components. However, the fitness function decreases rapidly with the number of generations and the optimized solution is found after almost 80 generations. The role of the three components is more evident from

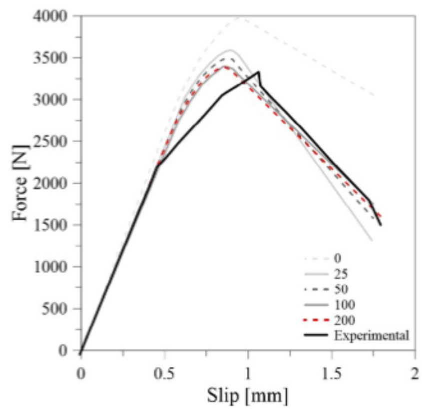

(a) Load-slip curves

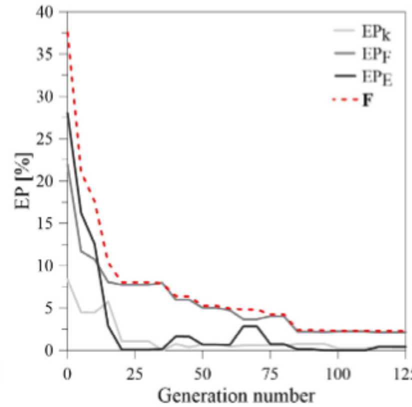

(b) EP values at different generations

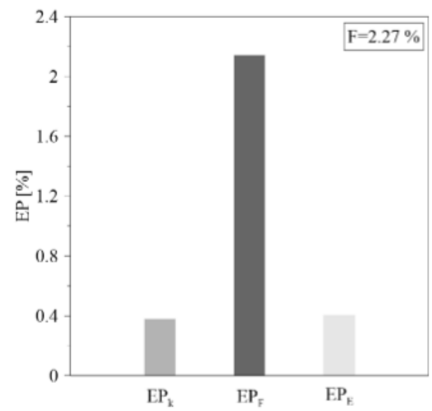

(c) Histogram of the EP values for the optimal solution

Fig. 13. Example of calibration based on the experimental results of [37].

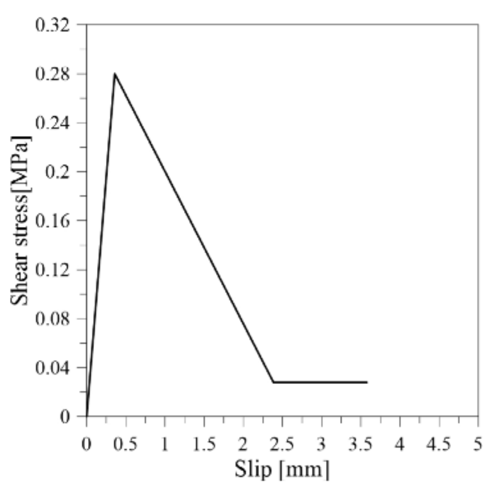

(a) Fabric-to-matrix interface

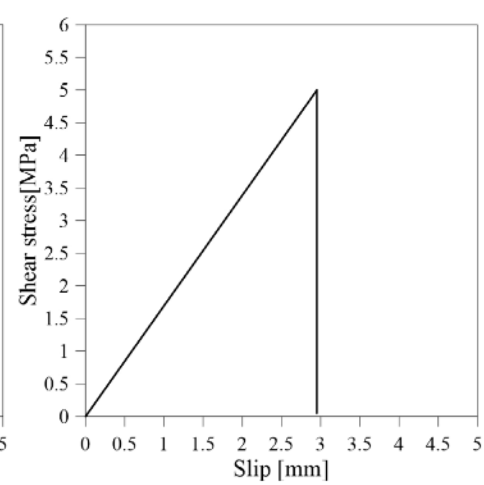

(b) Matrix-to-support interface

Fig. 14. Interfaces constitutive behavior.

Fig. 13(c), which shows the three percentage error contributions of the optimized solution. It is worth noting that very low values of error are found, with a final value of fitness equal to $F = 2.27\%$.

Finally, Fig. 14 shows the fibre-matrix 14(a) and matrix-support 14(b) interface behaviours, depending on the vector $\vec{V}_d$ obtained using the algorithm.

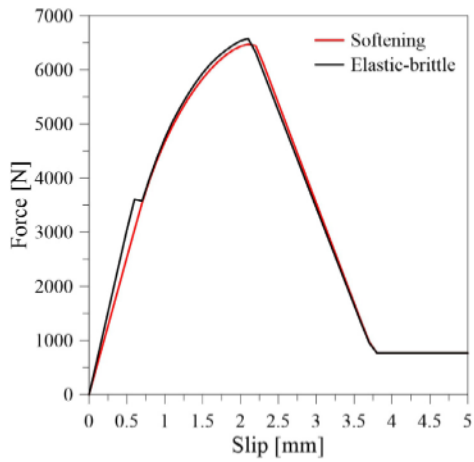

Fig. 15. Comparisons using two different constitutive behaviours.

5.2. Effect of a refined mortar constitutive law

In this section, it is clarified the role of a proper constitutive modelling of the softening effect in the mortar matrix. The results here considered refer to a sample from an experimental campaign performed by Rotunno et al. [39]. A cement-based mortar and a bi-directional PBO mesh make up the FRCM system. The mortar has a layer thickness of 4 mm, a flexural strength of 7.57 MPa, and a compressive strength of 32.5 MPa. While the fibre has an ultimate tensile strain of 2.5%, an equivalent thickness of 0.045 mm, and an elastic modulus of 253 GPa. The system's width was 63 mm, while the bond length was 315 mm. The number of elements per series was set at 50, resulting in a total of 150 truss elements, 200 ZeroLength element for brittle hinges and 153 ZeroLength elements to simulate the interfaces. Once again, the test was conducted under displacement control, setting a load increment equal to 0.05 mm. Fig. 15 shows the global force vs. slip curve obtained with two different models of the matrix. The curve in black was obtained by assuming a elastic pure brittle behaviour, with a maximum stress equal to mortar tensile strength, evaluated as the 10% of the compressive strength and equal to 3.25 MPa. While the red curve was obtained by introducing also an exponential softening branch (Fig. 4). This curves was evaluated though Eq. (9), setting the fracture energy value equal to 0.0073 N/mm. It is evident that no substantial differences are observed in this case and that the differences are however mainly limited to the first ascending branch of the curve.

5.3. Calibration against experimental database

In order to obtain a broad calibration of the interface parameters and simultaneously validate the model, the procedure was applied on results from an experimental database including 38 results taken from the literature. Appendix resumes the features of the specimens included in the database as well as the results of the calibration in tabular form. The specimens listed include different types of test set-ups, different geometry and type of constituent materials. The proposed procedure was run over all the experimental outcomes reported and the results are summarized in Figures from 16 to 28, which resume the comparisons between the optimally calibrated numerical simulations and the experimental Load vs. Slip curves for all the samples included in the database.

Fig. 16 shows the results of the experimental campaign conducted by Calabrese et al. [37] using the single lap direct shear test set up. The curves represent the results obtained by testing two samples with a cement-based matrix and two types of fibre: carbon and PBO. The response of these samples shows an initial linear branch until the formation of the first crack at the interface, which is followed by a non-linear phase characterized by a descending branch. The numerical curve well approximates this trend and the simulations showed that the second branch of the curve is governed by the softening branch attributed to the interface, in a manner consistent with what was observed experimentally.

A similar trend can be observed in Fig. 17, in which the experimental curves extracted from the experimental campaign of Turkmen et al. [38] are shown. The double shear bond tests set up, in this case, were conducted on specimens containing a carbon fibre mesh, and differing from each other only in the bond length. In this case the interface parameters obtained for the various simulations, specifically the maximum shear stress at the fibre-matrix interface and at the matrix-support interface, have values close to each other, as shown in the tabular results Appendix. Also in this case, the numerical model shows behaviour consistent with the experimental data. The specimens, during the test, exhibited a failure mode at the fibre-matrix interface with consequent slippage of the fibre, which on the numerical model is represented into a progressive failure of the interface springs, which assume stress values that are on the softening branch.

The same considerations apply to the curves in Fig. 18, which summarizes the results provided by Donnini and Corinaldesi [40], in which adhesion tests were conducted on samples with lime and carbon fibre-based mortar, differing in geometry, with double set-ups. It should be emphasized that in this case, in the curves obtained experimentally, the trend of the first branch was not well defined, so it was not easy to calculate the stiffness parameter required for the numerical simulations. Nevertheless, by means of the algorithm, good results were also obtained in this case, managing to simulate both the first linear branch and the descending post-peak branch with good approximation.

Similarly, the case shown in Fig. 19 reports the experimental results of Rotunno et al. [39] i.e. samples with carbon fibre tested with single lap shear test set up. The failure mode shown during the test is due to the sliding of the fabric within the matrix. The numerical model also approximates the response well in this case, exhibiting a horizontal final stretch, with constant load, resulting from the tangential interface springs reaching residual stress.

On the other hand, the curves reported in Fig. 20(a), belonging to the campaign conducted by Bellini and Mazzotti [41], show a quite different trend. In this case, the tests were conducted with a single-lap set-up, on samples made from carbon fibre and lime mortar, for which an adhesion promoter was used. A different trend is evident compared to the previous cases, in which the material initially exhibits linear behaviour until a force value is reached which triggers the delamination process, beyond which there is an increase in slip for constant force values. Also in this case the numerical model can simulate well the trend exhibited by the material during the test, managing to reproduce both the first linear branch and the post-cracking branch, with reduced differences in terms of force reached by the two curves.

The same trend is shown in Fig. 20(b), and also in this case the experimental curves show a post-peak branch with force values which are almost constant as the slip increases. For both cases the numerical model simulates well the trends exhibited by materials during the tests, managing to reproduce both the first linear branch and the following non-linear branch, with reduced differences in terms of force reached by the curves.

The same considerations apply to the curves in Fig. 21, which show the results of the experimental campaign conducted by Carozzi et al. [12] in the field of a round robin test framework. In this case, samples with carbon fibre were tested with a single-lap type test setup. The variability of the characteristics of the reinforcement, with the same type of support, has led to different experimental results. Moreover, in this case, it is possible to observe how well the model manages to simulate the behaviour, both in the case in which there is a post-cracking phase tending towards softening and in the case in which the sample exhibits different behaviour. The only case in which a good

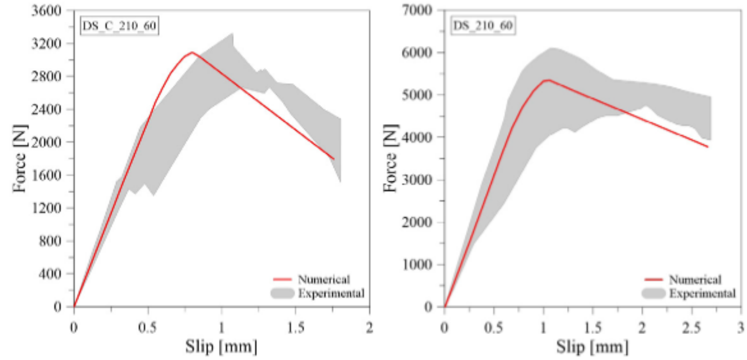

(a) Sample DS_C_210_60 (b) Sample DS_210_60

Fig. 16. Numerical-experimental comparisons: experimental campaign made by Calabrese et al. [37].

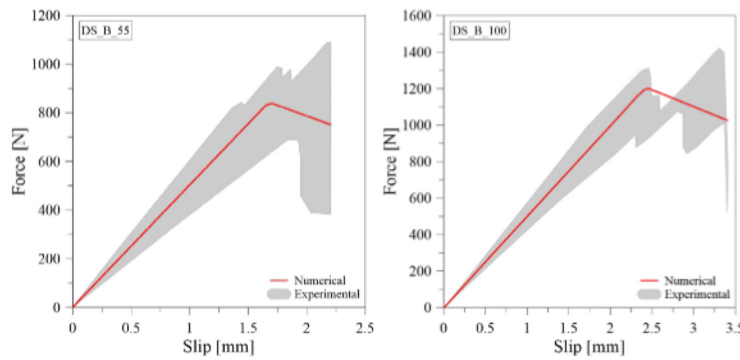

(a) Sample DS__B_55 (b) Sample DS__B_100

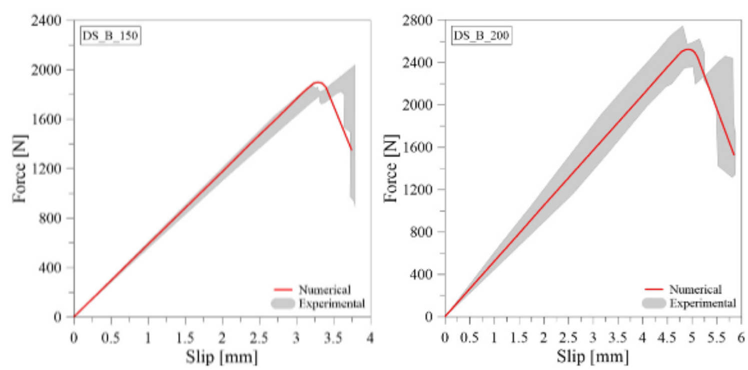

(c) Sample DS__B_150 (d) Sample DS__B_200

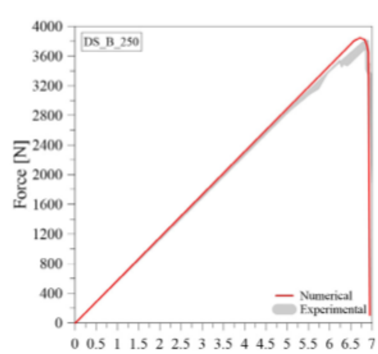

(e) Sample DS__B_250

Fig. 17. Numerical-experimental comparisons: experimental campaign made by Turkmen et al. [38].

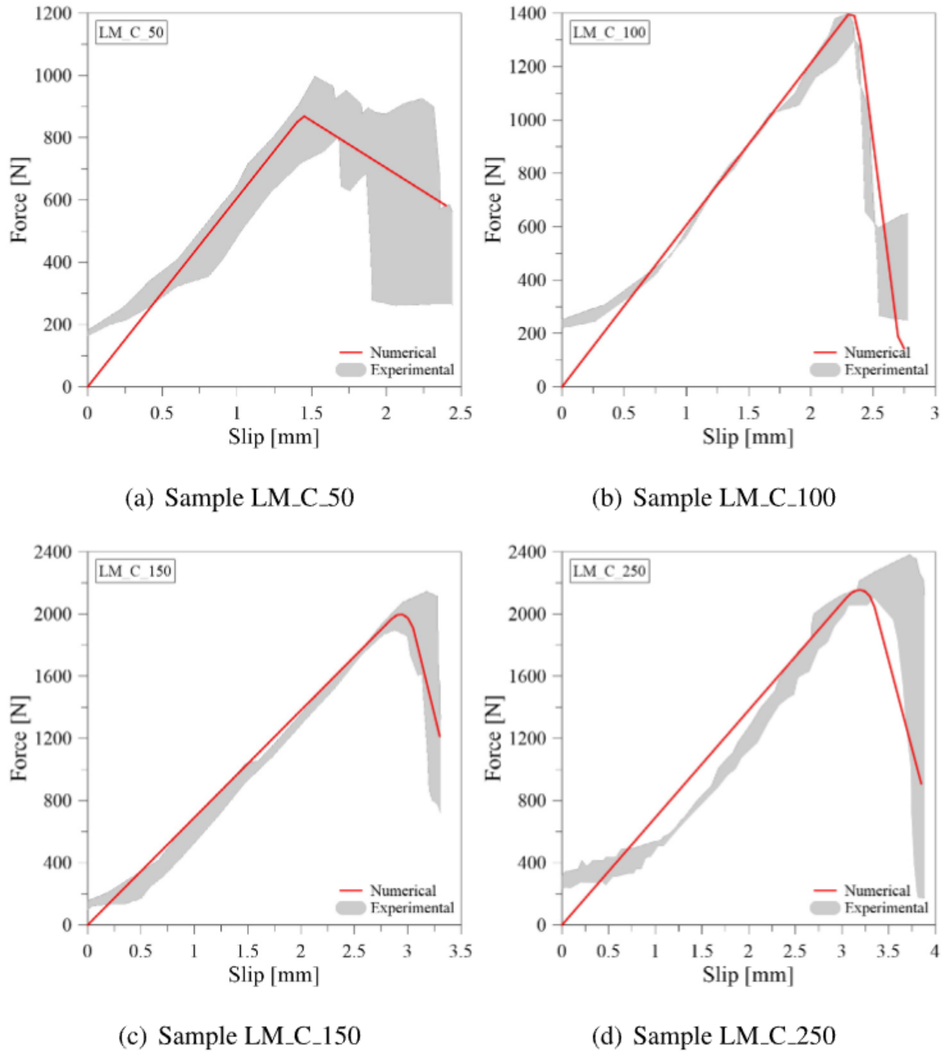

(a) Sample LM_C_50 (b) Sample LM_C_100

(c) Sample LM_C_150 (d) Sample LM_C_250

Fig. 18. Numerical-experimental comparisons: experimental campaign made by Donnini and Corinaldesi [40].

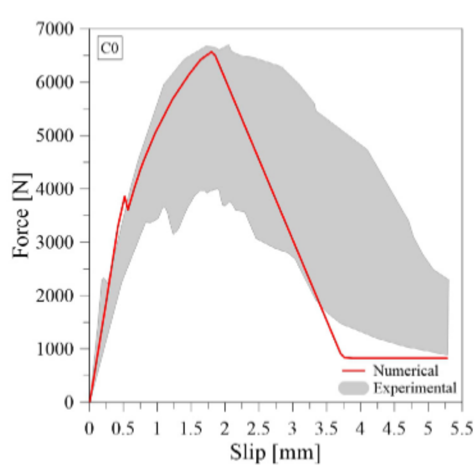

(a) Sample C0

Fig. 19. Numerical-experimental comparisons: experimental campaign made by Rotunno et al. [39].

agreement between numerical simulation and experimental result was not reached is the comparison shown in Fig. 21(d). In this example, although the numerical curve reproduces a similar trend to the experimental one, different load values are reached. It is important to underline that the data stated in the reference paper [12] were used as model input, i.e. values from technical data sheets, for both fibre and matrix. Moreover, it was stated by the researchers [12] that during the experimental campaign, the sample under investigation reached maximum stresses approximately 40% lower than those declared by manufacturer, both during tensile and shear-bond tests.

In general, therefore, it is possible to state that the algorithm thus implemented allows obtaining a good correspondence between the numerical and experimental results both concerning the first branch and the following post-cracking phase. It is useful to observe that the current trilinear shape of interface constitutive law is suitable to simulate the global behaviour of the specimen, both in the case in which a softening behaviour is exhibited and in the case in which a behaviour with hardening is exhibited (Figs. 22–28) .

The only case in which a good agreement between the two results has not been obtained is the case in Fig. 22(d). This may be due to the point chosen for the evaluation of the global stiffness. In fact, by observing the curves it is possible to see how in reality the numerical curve closely approximates the stiffness of the first branch of the experimental curves but fails to follow the trend of the curve in the

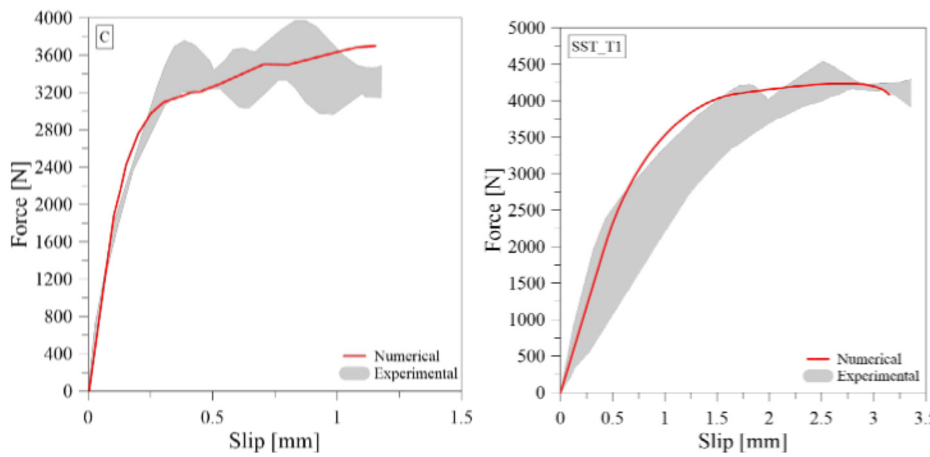

(a) Sample C (b) Sample SST_T1

Fig. 20. Numerical-experimental comparisons: experimental campaign made by Bellini and Mazzotti [41] and Ferrara et al. [42].

Table 1
Average experimental vs. numerical ratios.

	F_{num}/F_{exp}	E_{num}/E_{exp}	K_{num}/K_{exp}
Average	1.00	1.00	0.98
Standard deviation	0.04	0.04	0.06
COV (%)	4.06	4.37	6.24

subsequent branches, in which a slight difference in slope is evident. However, the trend of the experimental result shows a different trend compared to the case in the previous Fig. 22(c), for which the same type of FRCM was used and whose trend is instead well reproduced by the numerical simulation.

5.4. Correlations and optimized parameters

The quality of the calibration is resumed by the results shown in Fig. 29, which shows the comparisons between the experimental results (along the x-axis) and the optimized numerical solution (along the y-axis) in terms of maximum force, stiffness and dissipated energy (Figs. 29(a), 29(b), 29(c) respectively). It is evident that a good match is achieved through the calibration of the parameters, allowing to catch the main structural performance observed in the test.

More clearly, the same results have been summarized in Table 1. The ratio between numerical and the experimental values, in terms of stiffness, maximum force and dissipated energy, have been calculated for all the samples and, for each of them, the average value, standard deviation and Coefficient Of Variation (COV) have been reported in the table. It can be seen that the average values, in all the three cases, are very close to one, while the values of the coefficient of variation range from 4.06% to 6.24%. These results once again confirm the good match achieved through this type of calibration.

The parameters obtained from the updating procedures are therefore correlated to the main input parameters. Fig. 30(a) shows the maximum shear stress at the fm interface normalized with respect to the tensile strength of the mortar matrix f_{mt} for the different specimens included in the database.

It is worth observing as the maximum shear stress can be considered as a fraction of f_{mt}. On average the maximum shear stress is equal to almost the 15% of the matrix tensile strength, despite the value depends on the type of fibre, as evidenced by the figure. Only a few of specimens have maximum shear stress over $0.5f_{mt}$ and this is due to the application of an adhesion promoter over the dry fabric.

Fig. 30(b) shows the normalized maximum shear stress as a function of the mechanical ratio of fabric ω, this last defined as

$$\omega = \frac{A_f f_{ft}}{A_m f_{mt}} \tag{24}$$

It is worth noting that a linear correlation is found between the two parameters and the trend of the correlation depends on the type of fibre. It is also worth observing that the most of specimens have a ω value enclosed a limited range, almost lower than 7. Finally, Fig. 30(c) shows the trend of the interface shear stiffness $k_{c,fm}$ as a function of the relative ratio between the axial stiffness of the mortar and the that of fabric. An inverse trend is recorded in this case, stressing that the features of the interface are strongly influenced by both phases. In these last two figures, it was not possible to show a trend for the PBO fibre points, as there are only a few simulations performed.

6. Conclusions

This work presented the proposal of a GA-based procedure for the model updating of a FE model for predicting the bond behaviour of FRCM composites. The model is specifically formulated for minimizing the analysis time. The procedure is able to obtain the fabric-to-matrix and matrix-to-support parameters able to minimize the spread between the experimental result and the numerical simulation, through the formulation of an optimization problem. All the simulation and the updating procedure are integrated in an unique open-source environment, allowing to minimize the computation time and checking the results.

On the basis of the achieved results and for the range of key variables studied, the following conclusions can be drawn:

- the procedure works well over a database of 38 experimental results, matching the results on the global response in terms of Load vs. Slip curve; the variety of the experimental database proves the stability of the model for the different matrix-to-fabric combinations;
- the model is able to catch properly the different responses recorded experimentally along the post-peak phase, including linear brittle, softening and hardening response. This is possible by calibrating the parameters governing the interface laws, especially the slope of the descending branch;
- the procedure is rapidly convergent. The fitness function achieves values lower than 5% after few generations, without local minimum solutions; all the error measures expressed in the fitness function reach low values proving the efficacy of the proposed workflow;

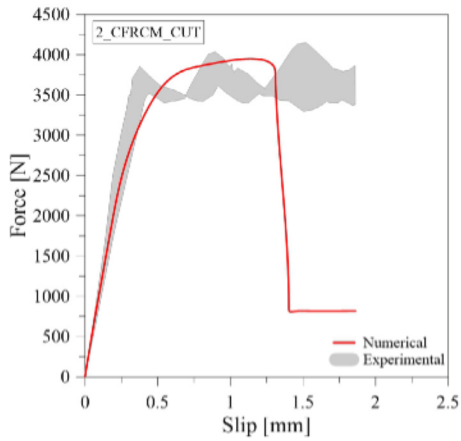

(a) Sample 2_CFRCM_CUT

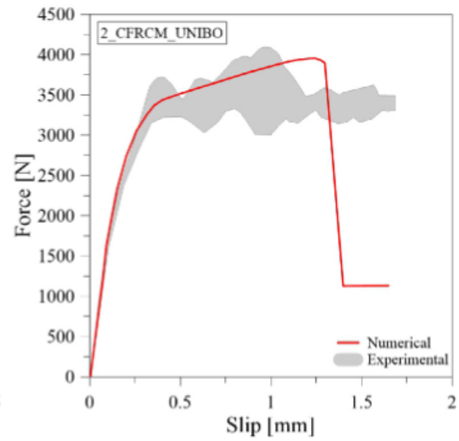

(b) Sample 2_CFRCM_UNIBO

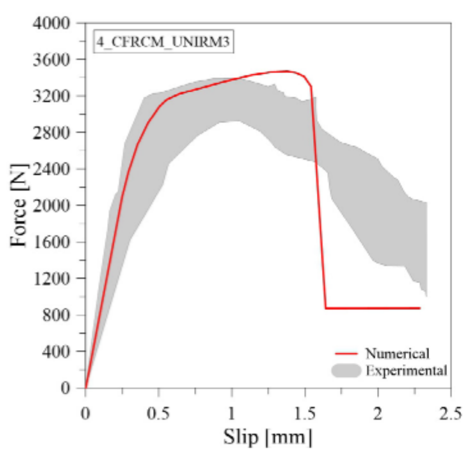

(c) Sample 4_CFRCM_UNIRM3

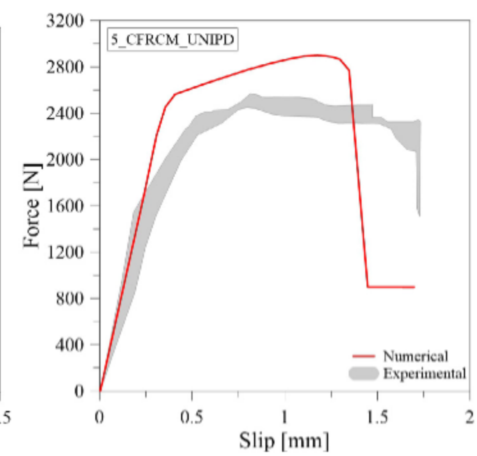

(d) Sample 5_CFRCM_UNIPD

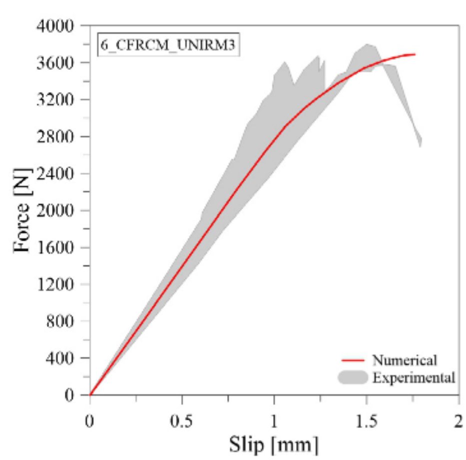

(e) Sample 6_CFRCM_UNIRM3

Fig. 21. Numerical-experimental comparisons: experimental campaign made by Carozzi et al. [12].

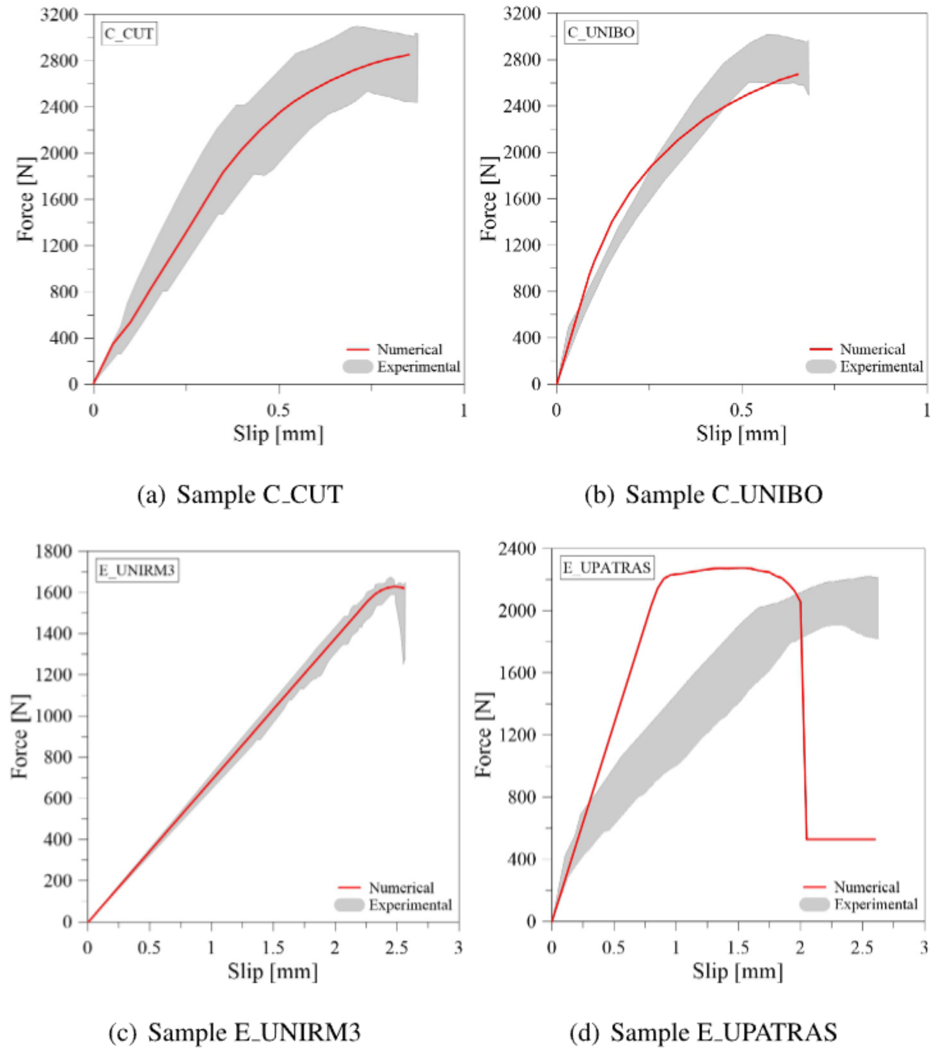

(a) Sample C_CUT (b) Sample C_UNIBO

(c) Sample E_UNIRM3 (d) Sample E_UPATRAS

Fig. 22. Numerical-experimental comparisons: experimental campaign made by Leone et al. [43].

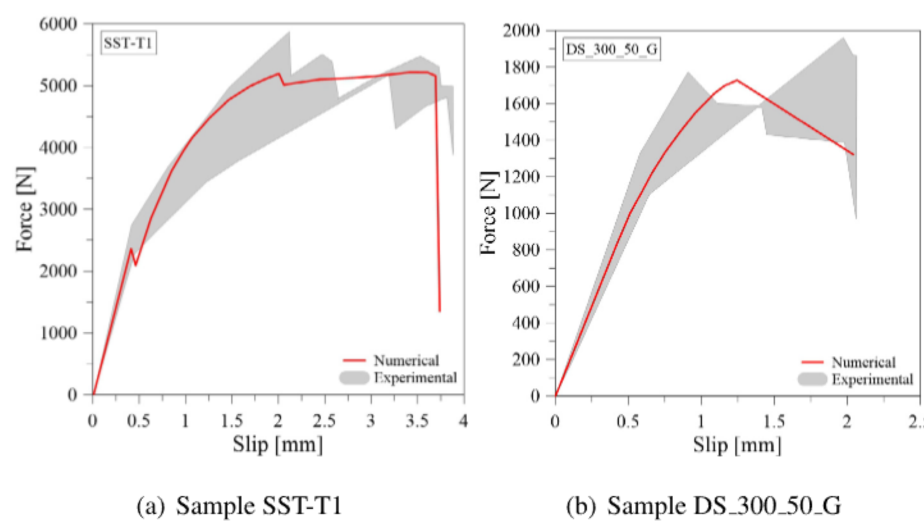

(a) Sample SST-T1 (b) Sample DS_300_50_G

Fig. 23. Numerical-experimental comparisons: experimental campaign made by De Santis et al. [44].

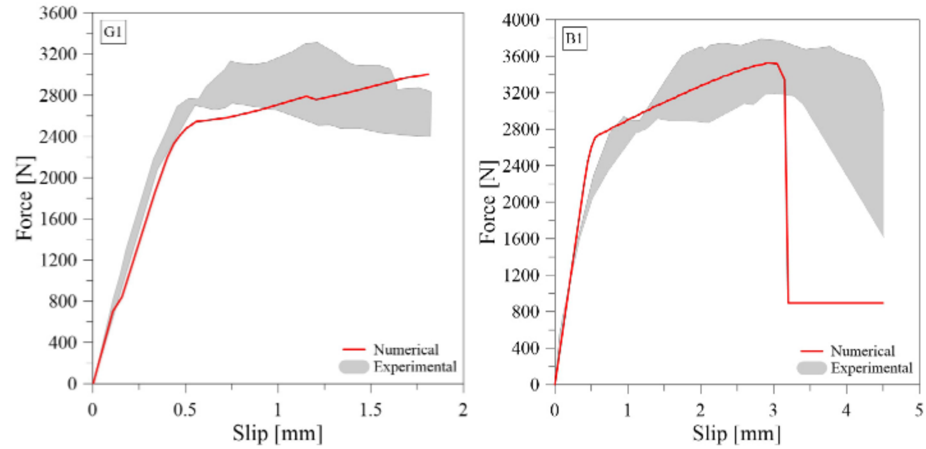

(a) Sample G1 (b) Sample B1

Fig. 24. Numerical-experimental comparisons: experimental campaign made by Bellini et al. [45].

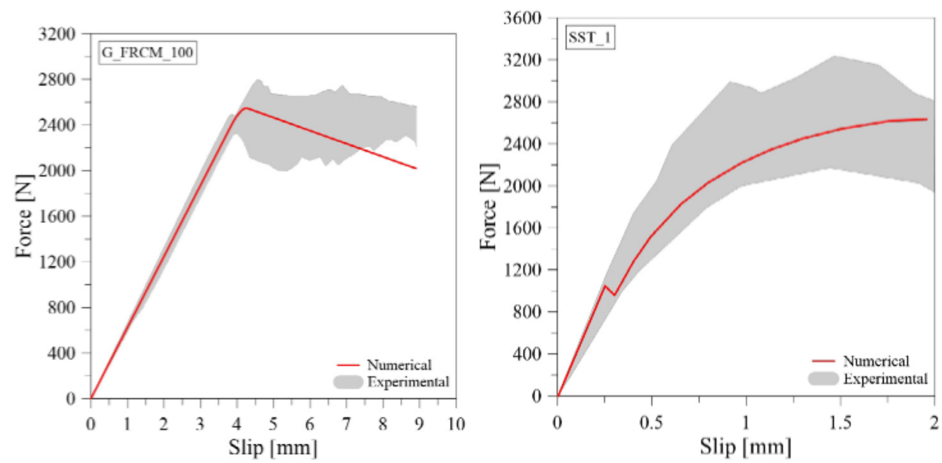

(a) Sample G_FRCM_100 (b) Sample SST1

Fig. 25. Numerical-experimental comparisons: experimental campaign made by Carozzi and Poggi [46] and Fazzi et al. [47].

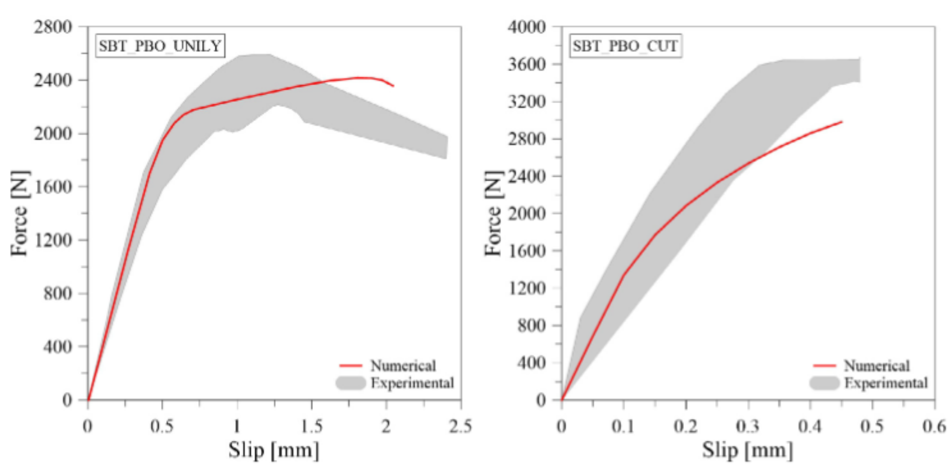

(a) Sample UNILY (b) Sample CUT

Fig. 26. Numerical-experimental comparisons: experimental campaign made by Caggegi et al. [48].

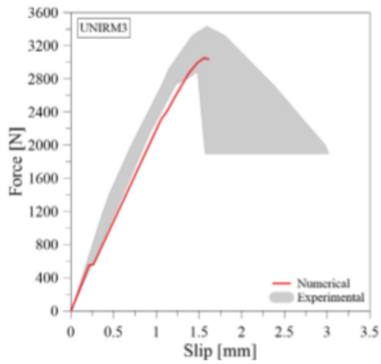

(a) Sample UNIRM3

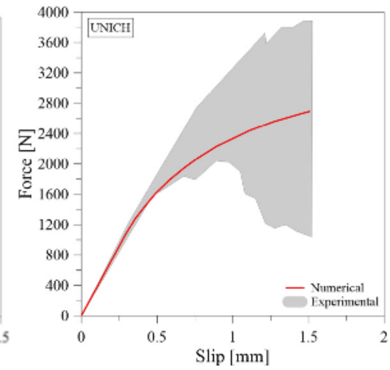

(b) Sample UNICH

Fig. 27. Numerical-experimental comparisons: experimental campaign made by Lignola et al. [49].

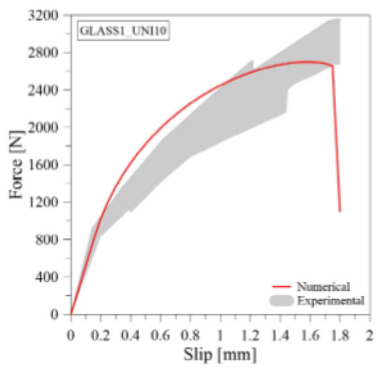

(a) Sample GLASS1_UNI10

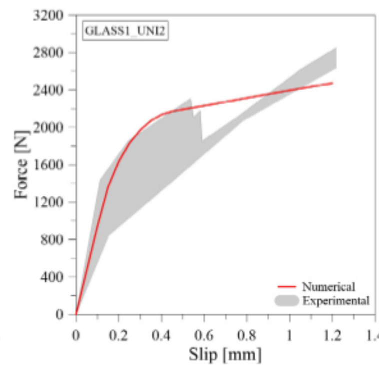

(b) Sample GLASS1_UNI2

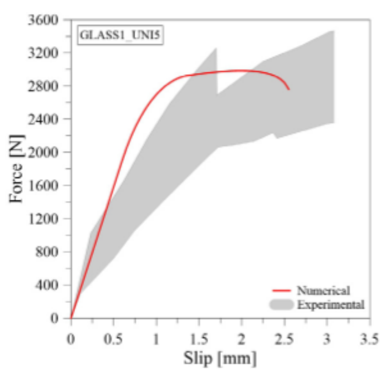

(c) Sample GLASS1_UNI5

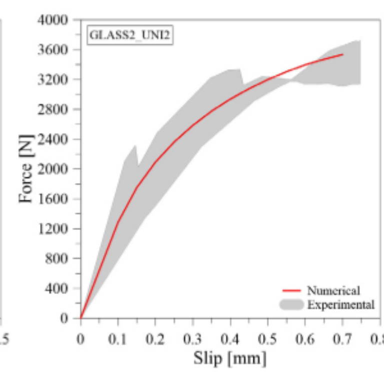

(d) Sample GLASS2_UNI2

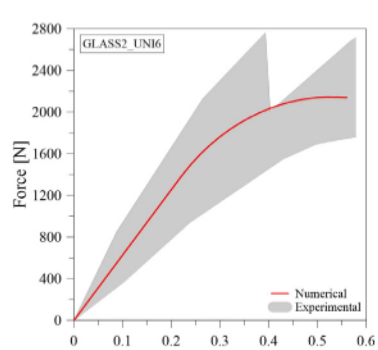

(e) Sample GLASS1_UNI6

Fig. 28. Numerical-experimental comparisons: experimental campaign made by Bellini et al. [15].

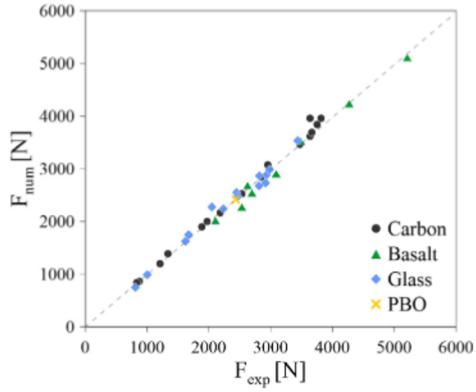

(a) Maximum force

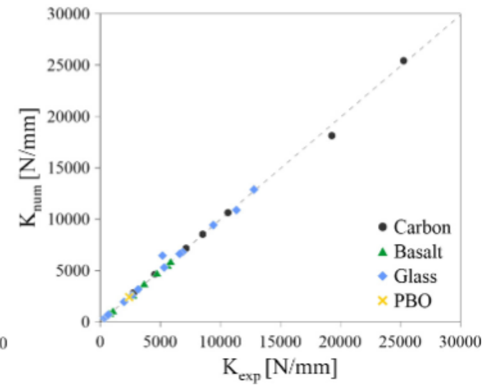

(b) Stiffness

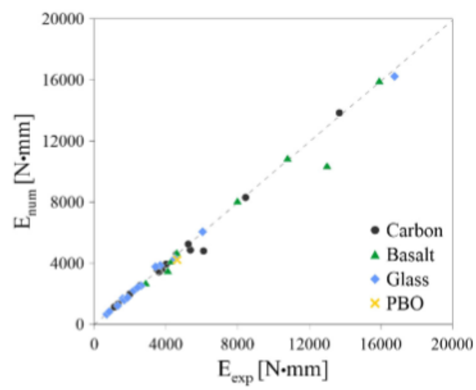

(c) Dissipated energy

Fig. 29. Experimental results vs. numerical predictions.

- the correlations of the calibrated parameters with the input variables show as the maximum shear stress at the interface can be considered always as a fraction of the tensile strength of the matrix, equal to 15% on average.

CRediT authorship contribution statement

Giovanni Minafò: Conceptualization, Methodology, Writing – original draft. **Marielisa Di Leto:** Data curation, Investigation, Validation. **Gaetano Camarda:** Formal analysis, Software, Visualization. **Lidia La Mendola:** Conceptualization, Supervision, Writing – review & editing.

Declaration of competing interest

All authors have participated in (a) conception and design, or analysis and interpretation of the data; (b) drafting the article or revising it critically for important intellectual content; and (c) approval of the final version.

This manuscript has not been submitted to, nor is under review at, another journal or other publishing venue.

The authors have no affiliation with any organization with a direct or indirect financial interest in the subject matter discussed in the manuscript.

Data availability

Data will be made available on request.

Acknowledgements

The study presented in this paper was developed within the activities of ReLUIS (Rete dei Laboratori Universitari di Ingegneria Sismica) for the project "Progetto Esecutivo Accordo DPC/Reluis 2022-2024" WP14–Contributi normativi per Materiali Innovativi per Interventi su Costruzioni Esistenti, funded by the Department for Civil Protection (DPC) of the Italian Presidency of the Ministers' Council.

This paper was produced while Marielisa Di Leto was attending the PhD programme in Advances In Modelling, Health-Monitoring, Infrastructures, Geomatics, Geotechnics, Hazards, Engineering Structures, Transportation (AIM HIGHEST), RETURN project, Spoke 3: VS3 - Earthquake and volcanoes, at the University of Palermo, Cycle XXXVIII, with the support of a scholarship financed by NRRP, funded by the European Union - NextGenerationEU - Mission 4 "Education and Research", Component 2 "From Research to Business" – Investment 1.3 "Creation of enlarged partnerships between universities, research centres, businesses and funding of basic research projects".

Appendix. Reference database

See Tables A.2 and A.3.

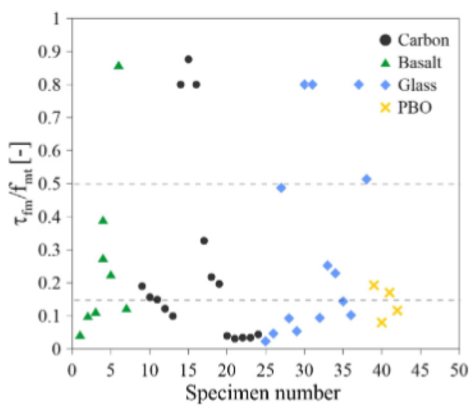

(a) Normalised maximum shear stress

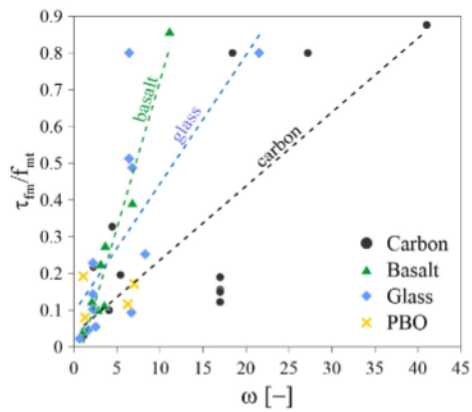

(b) Normalised maximum shear stress as a function of ω

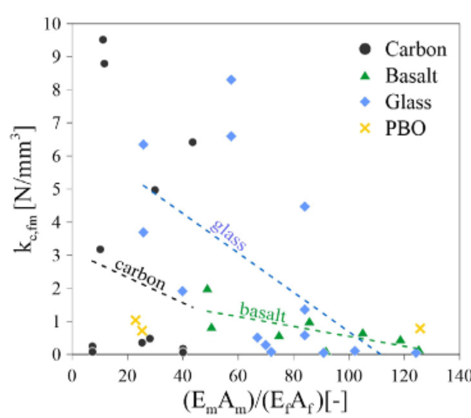

(c) interface shear stiffness as a function of the relative ratio between the axial stiffness of the mortar and the that of fabric.

Fig. 30. Correlations of optimized interface parameters.

Table A.2
Database of experimental results.

Sample id	Ref	Fabric		Matrix	
		E_f [GPa]	f_{ft} [MPa]	E_m [GPa]	f_{mt} [MPa]
BASALT					
SST_T1	[42]	56	1089	28.0	2.06
B1	[45]	70	1700	27.9	2.04
SST-T1	[44]	56	1089	25.7	1.60
SST_1	[47]	55	828	20.8	0.85
UNIRM3	[49]	71	1225	20.8	0.64
UNICH	[49]	51	802	20.8	1.50
CARBON					
LM_C_50	[40]	240	4900	9.0	1.50
LM_C_100	[40]	240	4900	9.0	1.50
LM_C_150	[40]	240	4900	9.0	1.50
LM_C_250	[40]	240	4900	9.0	1.50
DS_C_210_60	[37]	203	1944	29.9	2.50
C	[41]	240	2200	21.9	0.98
2_CFRCM_CUT	[12]	240	3400	19.1	0.65
2_CFRCM_UNIBO	[12]	240	3400	21.9	0.98
4_CFRCM_UNIRM3	[12]	197	1890	27.7	2.00
5_CFRCM_UNIPD	[12]	230	2500	34.3	3.80
6_CFRCM_UNIRM3	[12]	219	1890	25.9	1.64
DS_B_55	[38]	230	1700	40.5	6.26
DS_B_100	[38]	230	1700	40.5	6.26
DS_B_150	[38]	230	1700	40.5	6.26
DS_B_200	[38]	230	1700	40.5	6.26
DS_B_250	[38]	230	1700	40.5	6.26
GLASS					
G1	[45]	65	1000	25.0	1.47
G_FRCM_100	[46]	56	1233	30.7	2.71
DS_300_50_G	[50]	65	874	28.6	2.20
C_CUT	[43]	74	1400	19.1	0.65
C_UNIBO	[43]	74	1400	19.1	0.65
E_UNIRM3	[43]	70	2000	25.2	1.50
E_UPATRAS	[43]	70	2000	23.4	1.21
GLASS1_UNI2	[15]	68	968	28.6	2.20
GLASS1_UNI5	[15]	68	968	28.6	2.20
GLASS1_UNI10	[15]	68	968	28.6	2.20
GLASS2_UNI2	[15]	65	1131	22.4	1.06
GLASS2_UNI6	[15]	65	1131	22.4	1.06
PBO					
SBT_PBO_CUT	[48]	192	3356	36.1	4.43
SBT_PBO_UNILY	[48]	192	3356	33.7	3.61
DS_210_60	[37]	206	3040	29.9	2.50
C0	[39]	253	3610	32.6	3.25

Table A.3
Calibrated interface parameters.

Sample id	Fabric-to-matrix				Matrix-to-support	
	$\tau_{max,fm}$ [MPa]	s_1 [mm]	α_1 [–]	α_2 [–]	$\tau_{max,sm}$ [MPa]	s_2 [mm]
SST_T1	0.23	0.40	8.8	2.0	4.67	0.01
B1	0.80	0.40	1.60	2.0	4.81	0.20
SST-T1	0.44	0.44	4.6	1.1	5.00	1.73
SST_1	0.19	0.41	4.9	2.2	1.99	0.09
UNIRM3	0.55	0.65	2.0	2.0	2.11	2.56
UNICH	0.19	0.28	7.1	1.2	1.90	0.19
LM_C_50	0.29	1.20	3.3	1.9	2.52	1.91
LM_C_100	0.23	2.21	1.2	1.1	4.01	1.48
LM_C_150	0.23	2.80	1.3	1.3	2.68	0.64
LM_C_250	0.18	2.57	1.6	1.1	0.44	1.17
DS_C_210_60	0.25	0.52	5.4	1.1	4.53	0.01
C	0.79	0.08	4.0	1.6	5.00	0.01
2_CFRCM_CUT	0.57	0.18	4.1	1.5	4.24	0.02
2_CFRCM_UNIBO	0.78	0.09	4.8	1.7	5.00	0.01
4_CFRCM_UNIRM3	0.66	0.13	4.8	1.9	4.73	0.69
5_CFRCM_UNIPD	0.83	0.13	3.1	1.1	3.37	0.74
6_CFRCM_UNIRM3	0.32	0.90	3.3	1.9	3.00	0.02
DS_B_55	0.25	1.50	4.0	2.0	1.00	0.60
DS_B_100	0.20	2.16	3.8	1.1	0.86	0.85
DS_B_150	0.21	2.98	1.5	2.0	0.87	0.81
DS_B_200	0.21	4.50	1.5	2.0	0.87	0.81
DS_B_250	0.27	5.00	1.1	1.4	0.80	5.00
GC	0.09	2.21	1.2	1.1	0.40	2.49
GL	0.07	1.39	1.2	2.0	1.51	2.39
G1	0.72	0.38	1.6	2.0	5.00	0.01
G_FRCM_100	0.252	2.41	10.0	1.52	0.51	2.91
DS_300_50_G	0.12	0.43	10.0	1.1	4.16	0.01
C_CUT	0.52	0.14	6.6	1.7	4.83	1.76
C_UNIBO	0.52	0.08	10.0	1.9	5.00	0.01
E_UNIRM3	0.14	1.70	4.8	1.1	2.47	2.98
E_UPATRAS	0.31	0.61	1.1	1.9	4.98	0.49
GLASS1_UNI2	0.50	0.11	4.2	1.9	3.65	0.10
GLASS1_UNI5	0.32	0.55	2.5	1.9	3.65	0.82
GLASS1_UNI10	0.22	0.17	10.0	2.0	5.00	0.01
GLASS2_UNI2	0.84	0.10	9.0	1.3	5.00	0.01
GLASS2_UNI6	0.54	0.08	6.4	1.1	2.45	0.65
SBT_PBO_CUT	0.85	0.09	9.0	1.8	8.00	0.01
SBT_PBO_UNILy	0.29	0.37	2.0	1.4	5.00	0.36
DS_210_60	0.43	0.59	10.0	2.0	5.06	0.01
C0	0.38	0.36	10.0	2.0	4.88	0.01

(continued on next page)

References

[1] Nanni A. A new tool for concrete and masonry repair. Concr Int 2012;34(4):1–7.

[2] Amato G, Chen J, D'Anna J, La Mendola L, Minafò G. FRCM systems for strengthening masonry structures. In: 8th Biennial Conference on Advanced Composites in Construction, ACIC 2017. NetComposites Limited; 2017, p. 244–9.

[3] Monaco A, D'Anna J, Oddo MC, Minafò G, La Mendola L. Numerical modelling of the tensile behaviour of BFRCM strips. In: Key engineering materials. vol. 817, Trans Tech Publ; 2019, p. 15–22.

[4] Monaco A, Minafò G, D'Anna J, Oddo M, La Mendola L. Constitutive numerical model of FRCM strips under traction. Front Built Environ 2020;6:60.

[5] Incerti A, Ferretti F, Mazzotti C. FRCM strengthening systems efficiency on the shear behavior of pre-damaged masonry panels: an experimental study. J Build Pathol Rehabil 2019;4:1–13.

[6] Crisci G, Ceroni F, Lignola GP. Comparison between design formulations and numerical results for in-plane FRCM-strengthened masonry walls. Appl Sci 2020;10(14):4998.

[7] Meriggi P, de Felice G, De Santis S. Design of the out-of-plane strengthening of masonry walls with fabric reinforced cementitious matrix composites. Constr Build Mater 2020;240:117946.

[8] Minafò G, La Mendola L. Experimental investigation on the effect of mortar grade on the compressive behaviour of FRCM confined masonry columns. Composites B 2018;146:1–12.

[9] Aiello M, Bencardino F, Cascardi A, D'Antino T, Fagone M, Frana I, La Mendola L, Lignola G, Mazzotti C, Micelli F, et al. Masonry columns confined with fabric reinforced cementitious matrix (FRCM) systems: A round robin test. Constr Build Mater 2021;298:123816.

[10] Colombi P, D'Antino T. Analytical assessment of the stress-transfer mechanism in FRCM composites. Compos Struct 2019;220:961–70.

[11] Wang F, Kyriakides N, Chrysostomou C, Eleftheriou E, Votsis R, Illampas R. Experimental research on bond behaviour of fabric reinforced cementitious matrix composites for retrofitting masonry walls. Int J Concr Struct Mater 2021;15(1):1–17.

[12] Carozzi FG, Bellini A, D'Antino T, de Felice G, Focacci F, Hojdys Ł, Laghi L, Lanoye E, Micelli F, Panizza M, et al. Experimental investigation of tensile and bond properties of carbon-FRCM composites for strengthening masonry elements. Composites B 2017;128:100–19.

[13] Wang X, Lam C, Iu V. Bond behaviour of steel-TRM composites for strengthening masonry elements: Experimental testing and numerical modelling. Constr Build Mater 2020;253:119157.

[14] Carozzi FG, Arboleda D, Poggi C, Nanni A. Direct shear bond tests of fabric-reinforced cementitious matrix materials. J Compos Constr 2020;24(1).

[15] Bellini A, Aiello MA, Bencardino F, de Carvalho Bello CB, Castori G, Cecchi A, Ceroni F, Corradi M, D'Antino T, De Santis S, et al. Influence of different set-up parameters on the bond behavior of FRCM composites. Constr Build Mater 2021;308:124964.

[16] Calabrese A, D'Antino T, Colombi P. Experimental and analytical investigation of PBO FRCM-concrete bond behavior using direct and indirect shear test set-ups. Compos Struct 2021;267:113672.
[17] Al-Lami K, Calabrese AS, Colombi P, D'Antino T. Effect of wet-dry cycles on the bond behavior of fiber-reinforced inorganic-matrix systems bonded to masonry substrates. Materials 2021;14(20):6171.
[18] Grande E, Milani G. Interface modeling approach for the study of the bond behavior of FRCM strengthening systems. Composites B 2018;141:221–33.
[19] D'Antino T, Sneed LH, Carloni C, Pellegrino C. Influence of the substrate characteristics on the bond behavior of PBO FRCM-concrete joints. Constr Build Mater 2015;101:838–50.
[20] Bertolesi E, Grande E, Milani G. Numerical modeling of the bond behaviour of FRCM systems externally applied to masonry substrates. J Build Pathol Rehabil 2019;4(1):1–11.
[21] Calabrese AS, Colombi P, D'Antino T. Analytical solution of the bond behavior of FRCM composites using a rigid-softening cohesive material law. Composites B 2019;174:107051.
[22] Nerilli F, Marfia S, Sacco E. Micromechanical modeling of the constitutive response of FRCM composites. Constr Build Mater 2020;236:117539.
[23] Grande E, Milani G. Procedure for the numerical characterization of the local bond behavior of FRCM. Compos Struct 2021;258:113404.
[24] Zhu M, McKenna F, Scott MH. OpenSeesPy: Python library for the OpenSees finite element framework. SoftwareX 2018;7:6–11.
[25] Van Rossum G, Drake FL. Python 3 reference manual. CreateSpace; 2009.
[26] Oddo MC, Minafó G, Di Leto M, La Mendola L. Numerical modelling of the constitutive behaviour of FRCM composites through the use of truss elements. Materials 2023;16(3):1011.
[27] Minafò G, Oddo MC, Camarda G, Leto MD, La Mendola L. Effect of interface model parameters on the numerical response of a FE model for predicting the FRCM-to-masonry bond. Acta Mech 2023;1–15.
[28] EN 1992-1-1 Eurocode 2: Design of concrete structures - Part 1-1: General ruels and rules for buildings. Brussels: EN, CEN; 2005.
[29] Lourenço PB, Rots JG. Multisurface interface model for analysis of masonry structures. J Eng Mech 1997;123(7):660–8.
[30] Wang J, Jivkov AP, Li Q, Engelberg DL. Experimental and numerical investigation of mortar and ITZ parameters in meso-scale models of concrete. Theor Appl Fract Mech 2020;109:102722.
[31] Yuan Y, Milani G. Non-linear analytical model for FRCM coupons in tension. Composites B 2023;260:110735.
[32] Kubalık J, Lažanskỳ J. Genetic algorithms and their testing. In: AIP conference proceedings. volume 465, American Institute of Physics; 1999, p. 217–29.
[33] Michalewicz Z. Heuristic methods for evolutionary computation techniques. J Heuristics 1996;1:177–206.
[34] Vose MD. The simple genetic algorithm: Foundations and theory. MIT Press; 1999.
[35] Harris CR, Millman KJ, van der Walt SJ, Gommers R, Virtanen P, Cournapeau D, Wieser E, Taylor J, Berg S, Smith NJ, Kern R, Picus M, Hoyer S, van Kerkwijk MH, Brett M, Haldane A, del Río JF, Wiebe M, Peterson P, Gérard-Marchant P, Sheppard K, Reddy T, Weckesser W, Abbasi H, Gohlke C, Oliphant TE. Array programming with NumPy. Nature 2020;585(7825):357–62. http://dx.doi.org/10.1038/s41586-020-2649-2.
[36] Hunter JD. Matplotlib: A 2D graphics environment. Comput Sci Eng 2007;9(3):90–5. http://dx.doi.org/10.1109/MCSE.2007.55.
[37] Calabrese AS, D'Antino T, Colombi P, Poggi C. Study of the influence of interface normal stresses on the bond behavior of FRCM composites using direct shear and modified beam tests. Constr Build Mater 2020;262:120029.
[38] Turkmen O, de Vries B, Wijte S. Mechanical characterization and out-of-plane behaviour of fabric reinforced cementitious matrix (FRCM) overlay on clay brick masonry. Civil Eng Des 2019;1.
[39] Rotunno T, Fagone M, Grande E, Milani G. FRCM-to-masonry bonding behaviour in the case of curved surfaces: experimental investigation. Compos Struct 2023;313:116913.
[40] Donnini J, Corinaldesi V. Mechanical characterization of different FRCM systems for structural reinforcement. Constr Build Mater 2017;145:565–75.
[41] Bellini A, Mazzotti C. Bond behavior and tensile properties of FRCM composites applied on masonry panels. 2016.
[42] Ferrara G, Caggegi C, Gabor A, Martinelli E. Experimental study on the adhesion of basalt textile reinforced mortars (TRM) to clay brick masonry: the influence of textile density. Fibers 2019;16(3):1011.
[43] Leone M, Aiello MA, Balsamo A, Carozzi FG, Ceroni F, Corradi M, Gams M, Garbin E, Gattesco N, Krajewski P, Mazzotti C, Oliveira D, Papanicolaou C, Ranocchiai G, Roscini F, Saenger D. Glass fabric reinforced cementitious matrix: tensile properties and bond performance on masonry substrate. Composites B 2017;127:196–214.
[44] De Santis S, de Felice G, Roscini F. Retrofitting of masonry vaults by basalt textile-reinforced mortar overlays. Eur J Environ Civ Eng 2021.
[45] Bellini A, Shareza SK, mazzotti C. Cyclic bond nehavior of FRCM composites applied on masonry substrate. Composites B 2019;169:189–99.
[46] Carozzi FG, Poggi C. Mechanical properties and debonding strength of fabric reinforced cementitious matrix (FRCM) systems for masonry strengthening. Composites B 2015;70:215–30.
[47] Fazzi E, Misseri G, Rovero L. Experimental, analytical, and numerical investigations on bond behaviour of basalt TRM systems. Int J Mason Res Innov 2023;8(2–3):333–54.
[48] Caggegi C, Carozzi FG, De Santis S, Fabbrocino F, Focacci F, Hojdys L, Lanoye E. Experimental analysis on tensile and bond properties of PBO and aramid fabric reinforced cementitious matrix for strengthening masonry structures. Composites B 2017;127:175–95.
[49] Lignola GP, Caggegi C, Ceroni F, De Santis S, Krajewski P, Lourenco PB, Morganti M, Papanicolaou C, Pellegrino C, Prota A, Zuccarino L. Performance assessment of basalt FRCM for retrofit applications on masonry. Composites B 2017;128:1–18.
[50] Al-lami K, D'Antino T, Colombi P. Study of the bond capacity of FRCM and SRG masonry joints. CivilEng 2021;(2):68–86.